

The role of anthropogenic aerosol forcing in the 1850-1985 strengthening of the AMOC in CMIP6 historical simulations

Article

Published Version

Creative Commons: Attribution 4.0 (CC-BY)

Open access

Robson, Jon ORCID logo ORCID: <https://orcid.org/0000-0002-3467-018X>, Menary, Matthew B., Sutton, Rowan T. ORCID logo ORCID: <https://orcid.org/0000-0001-8345-8583>, Mecking, Jenny, Gregory, Jonathan M., Jones, Colin, Sinha, Bablu, Stevens, David P. and Wilcox, Laura J. ORCID logo ORCID: <https://orcid.org/0000-0001-5691-1493> (2022) The role of anthropogenic aerosol forcing in the 1850-1985 strengthening of the AMOC in CMIP6 historical simulations. *Journal of Climate*, 35 (20). pp. 3243-3263. ISSN 1520-0442 doi: <https://doi.org/10.1175/JCLI-D-22-0124.1> Available at <https://centaur.reading.ac.uk/105935/>

It is advisable to refer to the publisher's version if you intend to cite from the work. See [Guidance on citing](#).

To link to this article DOI: <http://dx.doi.org/10.1175/JCLI-D-22-0124.1>

Publisher: American Meteorological Society

All outputs in CentAUR are protected by Intellectual Property Rights law, including copyright law. Copyright and IPR is retained by the creators or other copyright holders. Terms and conditions for use of this material are defined in

the [End User Agreement](#).

www.reading.ac.uk/centaur

CentAUR

Central Archive at the University of Reading

Reading's research outputs online

The Role of Anthropogenic Aerosol Forcing in the 1850–1985 Strengthening of the AMOC in CMIP6 Historical Simulations

JON ROBSON,^a MATTHEW B. MENARY,^b ROWAN T. SUTTON,^a JENNY MECKING,^c JONATHAN M. GREGORY,^{a,d} COLIN JONES,^e BABLU SINHA,^c DAVID P. STEVENS,^f AND LAURA J. WILCOX^a

^a National Centre for Atmospheric Science, Department of Meteorology, University of Reading, Reading, United Kingdom

^b LOCEAN, Sorbonne Université, Paris, France

^c National Oceanography Centre, Southampton, United Kingdom

^d Met Office Hadley Centre, Met Office, Exeter, United Kingdom

^e National Centre for Atmospheric Science, University of Leeds, Leeds, United Kingdom

^f Centre for Ocean and Atmospheric Sciences, School of Mathematics, University of East Anglia, Norwich, United Kingdom


(Manuscript received 25 February 2022, in final form 1 June 2022)


ABSTRACT: Previous work has shown that anthropogenic aerosol (AA) forcing drives a strengthening in the Atlantic meridional overturning circulation (AMOC) in CMIP6 historical simulations over 1850–1985, but the mechanisms have not been fully understood. Across CMIP6 models, it is shown that there is a strong correlation between surface heat loss over the subpolar North Atlantic (SPNA) and the forced strengthening of the AMOC. Despite the link to AA forcing, the AMOC response is not strongly related to the contribution of anomalous downwelling surface shortwave radiation to SPNA heat loss. Rather, the spread in AMOC response is primarily due to the spread in turbulent heat loss. We hypothesize that turbulent heat loss is larger in models with strong AA forcing because the air advected over the ocean is colder and drier, in turn because of greater AA-forced cooling over the continents upwind, especially North America. The strengthening of the AMOC also feeds back on itself positively in two distinct ways: by raising the sea surface temperature and hence further increasing turbulent heat loss in the SPNA, and by increasing the sea surface density across the SPNA due to increased northward transport of saline water. A comparison of key indices suggests that the AMOC response in models with strong AA forcing is not likely to be consistent with observations.

KEYWORDS: North Atlantic Ocean; Meridional overturning circulation; Thermocline circulation; Aerosols; Coupled models

1. Introduction

The Atlantic meridional overturning circulation (AMOC) is an important component of Earth's climate. It plays a key role in the poleward transport of heat within the Northern Hemisphere (Trenberth et al. 2019) and across the equator (Marshall et al. 2014) and is correlated with the sequestration of heat and carbon in the deep ocean (Sarmiento and Le Quéré 1996; Kostov et al. 2014). Moreover, a range of observational, paleo, and modeling work has linked changes in the strength of the AMOC, and related ocean heat transports, to a long list of regional and global climate impacts including impacts on sea surface temperature (SST), rainfall, hurricanes, and sea level (Yin et al. 2009; Zhang et al. 2019; Bellomo et al. 2021). Therefore, it is important to improve our understanding of how the AMOC can shape regional and global climate in order to reduce uncertainty in climate predictions.

 Denotes content that is immediately available upon publication as open access.

 Supplemental information related to this paper is available at the Journals Online website: <https://doi.org/10.1175/JCLI-D-22-0124.s1>.

Corresponding author: Jon Robson, j.i.robson@reading.ac.uk

The AMOC is known to vary on a range of time scales and due to a range of processes. For example, changes in the strength of the wind stress are known to be important on daily to decadal time scales through its impact on Ekman currents and Ekman upwelling/downwelling (Polo et al. 2014; Blaker et al. 2015; Buckley and Marshall 2016; Jackson et al. 2022). AMOC variability on decadal and longer time scales has often been linked to changes in surface buoyancy fluxes and their impact on dense water formation in the North Atlantic (Robson et al. 2012; Grist et al. 2014; Gregory et al. 2016; Delworth and Zeng 2016; Xu et al. 2019; Yeager et al. 2021; Megann et al. 2021; Jackson et al. 2022). Climate models indicate that internal variability is an important source of AMOC variability on daily to centennial time scales (Buckley and Marshall 2016; Jackson et al. 2022). However, changes in natural and anthropogenic external forcings can also drive AMOC variability. For example, changes in solar radiation and volcanic emissions have been shown to induce decadal-to-multidecadal variability in the AMOC (Otterå et al. 2010; Menary and Scaife 2014; Swingedouw et al. 2015). In the future, the AMOC is expected to weaken significantly as an increasingly warmer climate weakens the surface buoyancy forcing of the AMOC (Weijer et al. 2020; Couldrey et al. 2021).



This article is licensed under a [Creative Commons Attribution 4.0 license](http://creativecommons.org/licenses/by/4.0/) (<http://creativecommons.org/licenses/by/4.0/>).

DOI: 10.1175/JCLI-D-22-0124.1

© 2022 American Meteorological Society. For information regarding reuse of this content and general copyright information, consult the [AMS Copyright Policy](https://www.ametsoc.org/PUBSReuseLicenses/) (www.ametsoc.org/PUBSReuseLicenses/).

A recent focus has been on understanding the relative role of different anthropogenic forcings in explaining past AMOC change. In particular, over the historical period there has been a competition between greenhouse gas (GHG) forcing and anthropogenic aerosol (AA) forcing. Many studies have highlighted that AA forcing can have a large impact on the North Atlantic, and AA forcing has been shown to strengthen the AMOC in climate models (Cai et al. 2006; Delworth and Dixon 2006; Menary et al. 2013; Undorf et al. 2018; Andrews et al. 2020; Menary et al. 2020; Robson et al. 2020; Hassan et al. 2021; Fiedler and Putrasahan 2021). Previously these competing anthropogenic effects were thought to lead to relatively little externally forced change over the historical period (Delworth and Dixon 2006; Cheng et al. 2013). However, some models with strong AA forcing were known to have an increase in AMOC (Menary et al. 2013). More recently, Menary et al. (2020) showed that the multimodel mean AMOC increased significantly over 1850–1985 in historical simulations made for phase 6 of the Coupled Modeling Intercomparison Project (CMIP6). Furthermore, Menary et al. (2020) attributed the AMOC increase to stronger AA forcing in CMIP6 compared to CMIP5, primarily due to the inclusion of aerosol–cloud interactions in more models. However, the increase in the historically simulated AMOC in CMIP6 is in stark contrast to observation- or paleo-based proxies of the AMOC that indicate it has already declined significantly (Thornalley et al. 2018; Caesar et al. 2018, 2021). As one interpretation of this mismatch is that models do not adequately represent the sensitivity of AMOC to historical anthropogenic forcing, there is a pressing need to further understand the simulation of historical AMOC.

Unfortunately, there are few studies that have explored *how* AA affects the AMOC; furthermore, those studies highlight different mechanisms. For example, Delworth and Dixon (2006) and Menary et al. (2013) both focus on an analysis of upper ocean density anomalies and argue that AA forcing drives AMOC through changes in upper ocean salinity. However, Delworth and Dixon (2006) attribute salinity changes to decreased high-latitude precipitation, whereas Menary et al. (2013) attribute it to increased evaporation driven by atmospheric circulation changes. Furthermore, neither study explores the role of surface heat flux (SHF). In contrast, Hassan et al. (2021) took a surface density flux approach and attributed the multimodel mean AMOC increase in CMIP6 to changes in SHF. In particular, they argued that the AMOC strengthening was driven primarily by reduced downwelling shortwave radiation and wind-driven changes in turbulent heat fluxes. Menary et al. (2020) have also highlighted that the AMOC changes were consistent with interhemispheric energy constraints, but they performed no evaluation relative to other mechanisms.

All these studies also explore the mechanism in only one model (e.g., Delworth and Dixon 2006; Menary et al. 2013) or in the multimodel mean (e.g., Menary et al. 2020; Hassan et al. 2021). However, the magnitude of AA forcing is highly uncertain in terms of magnitude and both spatial and temporal variability (Zelinka et al. 2014; Smith et al. 2021). Furthermore, due to the contemporaneous and competing external forcings

it is not clear whether the dominant mechanisms are the same for all time periods (Menary et al. 2020; Hassan et al. 2021; Kang et al. 2021). Finally, models are also known to suffer from a range of biases in surface climate and AMOC that may affect the response (Wang et al. 2014; Menary et al. 2015; Jackson et al. 2020). Therefore, a range of questions remain about how AA may have shaped the evolution of the AMOC in the real world.

The goal of this study is, therefore, to better understand how AA forcing drives the AMOC across CMIP6 models. We do this by exploring the range of simulated AMOC responses by contrasting the difference between models with strong or weak sensitivity to AA forcing. In particular, we focus on the period 1850–1985 as this is the time period over which Menary et al. (2020) attributed AA forcing as the primary driver of externally forced AMOC change in CMIP6. After this period the role of AA forcing becomes less clear, likely due in part to the increasingly important role of GHG forcing (Menary et al. 2020) and the more complex changes in AA forcing (i.e., large regional changes but small global changes; Dittus et al. 2021; Kang et al. 2021). As in Hassan et al. (2021), we focus on understanding the forced response in a surface density flux framework (i.e., the role of surface heat and freshwater fluxes in driving AMOC) and focus exclusively on CMIP6 simulations.

The paper is structured as follows. An overview of data and analysis methods is included in section 2. Analyses of surface density fluxes and surface heat fluxes are presented in section 3 and section 4, respectively. In section 5 we discuss the importance of continental regions for mediating the response of the AMOC to AA forcing, and section 6 discusses evidence of important feedbacks for the AMOC response. A discussion of the results, including a comparison with observations, is presented in section 7. We conclude in section 8 with a summary of the key results.

2. Data and methods

a. CMIP6 historical simulations

We explore the externally forced changes in AMOC by using the historical simulations made for CMIP6 (Eyring et al. 2016). These simulations include time-varying changes in external forcings due to both natural (e.g., solar and volcanic aerosols) and anthropogenic sources (e.g., well-mixed greenhouse gases, anthropogenic aerosol and their precursors, and land use change). For further details of the historical simulations we direct the reader to Eyring et al. (2016). We include 17 CMIP6 models in total (see the online supplemental material for model details and references). These models were chosen as they include most of the variables that we analyze for at least three members. To ensure models have similar numbers of ensemble members, and to simplify data analysis, we also use only the first nine members of any individual model. Overall we use 113 individual realizations (see Table S1 in the online supplemental material).

b. Diagnostics and observational data

The model data used in this study were retrieved from the CMIP6 archive. Before analysis, all model data were

regridded to a $2.5^\circ \times 2.5^\circ$ latitude–longitude grid in order to aid comparison. As we focus on the externally forced changes, we analyze ensemble means of individual models or multimodel means (except in the analysis presented in Fig. 12), and the time series are smoothed with a 10-yr running mean.

As in Menary et al. (2020), we focus on the AMOC at 35°N computed in z coordinates, but this latitude is representative of the wider Atlantic [see Menary et al. (2020) for details]. To ensure consistency across models, all AMOC data were generated directly from ocean velocities, except for NorESM2-LM, which uses potential density as the vertical coordinate for the ocean and, hence, CMIP6 variable *msfyz* (ocean mass streamfunction in Y) was used instead. As shown in Menary et al. (2020), the AMOC indices computed from ocean velocities capture the annual AMOC variability when compared to *msfyz* and the subsequent results are not sensitive to this choice [see Menary et al. (2020) for further details of the evaluation of AMOC indices].

We use the CMIP6 variable *hfds* for net surface heat fluxes into the ocean (which we refer to as SHF). Note that *hfds* was not available in some models (BCC-CSM2-MR, INM-CM5-0, and MIROC6). For these models, anomalies have been reconstructed using heat flux components from the atmospheric grid (e.g., turbulent and radiative heat fluxes). Although we do not include all terms, such as those associated with sea ice, we find that correlations of the decadal smoothed reconstructed SHF and *hfds* averaged over the subpolar North Atlantic for models with both available are >0.95 (not shown), implying that we are capturing the majority of heat flux variability. Averages in variables over regions of the ocean were computed after a land–sea mask was applied.

Surface density fluxes, and specifically the thermal and haline components, are computed here using the standard equations [e.g., following Speer and Tziperman (1992)]. Due to the spread in model climatologies of sea surface temperature and salinity (not shown) we use fixed constants for the thermal and haline expansion coefficients which allows us to quickly compare the magnitude of surface density flux anomalies. Specifically, we use $\alpha = -1.4 \times 10^{-3} \text{ K}^{-1}$ and $\beta = 0.8 \times 10^{-3} \text{ ppt}^{-1}$ (ppt = parts per thousand) to compute subpolar North Atlantic surface density flux based on Fig. 1 from Griffies et al. (2014). Note that broad conclusions on the relative importance of thermal compared to haline components presented in section 3 are not sensitive to the exact values of α and β . The salinity and temperature components of surface density anomalies are computed by holding the other variables at a monthly varying climatology (Delworth et al. 1993). All climatologies, unless otherwise stated, are for the period 1850–79.

We also compare some of the key variables with observations. SST data are taken from ERSST v5 (Huang et al. 2017). Subpolar salinity data are taken from the “annually binned sea surface salinity” dataset of Reverdin et al. (2019). Note that to define the observed subpolar North Atlantic (SPNA) sea surface salinity (SSS) time series we simply take the unweighted average of anomalies over all grid boxes north of 45°N in the observational salinity dataset, due to the use of an irregular grid in this dataset. (This is not the case for other datasets, where we use an average over the regions specified weighted by grid area.)

The surface air temperature data are taken from Berkeley Earth surface temperature dataset (BEST; Rohde and Hausfather 2020).

c. Stratification of models into subensembles based on interhemispheric energy imbalance

Menary et al. (2020) showed that the strength of the externally forced AMOC change over 1850–1985 in CMIP5 and CMIP6 historical simulations was largely proportional to the interhemispheric difference in the absorbed (or net) solar radiation at the top of the atmosphere (which they called ASR_HD). In particular, they defined the ASR_HD index as the Southern Hemisphere mean net shortwave minus the Northern Hemisphere mean net shortwave, so that positive values indicate that less solar radiation is absorbed in the Northern Hemisphere (as incoming radiation is the same in the two hemispheres). Furthermore, they showed that an increase in the ASR_HD index over 1850–1985 was associated with an increase in AMOC, whereas a decrease over 1985–2014 was associated with a weakening AMOC. Using single-forcing simulations made for the Detection and Attribution Model Intercomparison project (DAMIP; Gillett et al. 2016), Menary et al. (2020) also showed that for ~ 1850 –1985, the changes in the ASR_HD index were primarily controlled by changes in the AA forcing (see their Fig. 2). However, after 1985 the relationship became more complicated with both AA and GHG forcing contributing.

We take advantage of the relationship between ASR_HD and AMOC changes in order to stratify models into subensembles that have so-called strong and weak responses to aerosol forcing over the period 1850–1985. Specifically, we split models into those that simulate a linear change in ASR_HD over 1850–1985 that is larger than 1.5 W m^{-2} based on a linear regression (which we name “strong”) and those that have a smaller change (which we name “weak”). We do this by fitting a linear trend to the ensemble-mean time series and multiplying by the number of years between 1850 and 1985 (i.e., 136). Note that 1.5 W m^{-2} is an arbitrary choice in order to have comparable sized subensembles (9 models and 55 members for strong, and 8 models and 58 members for weak) but the results are not sensitive to this exact threshold.

Figure 1 shows the resulting time series of ASR_HD and the AMOC at 35°N as well as the relationship in their linear trends over the period 1850–1985. For the multimodel mean (MMM) there is an increase in both ASR_HD and the AMOC from 1850 to 1985 with the fastest increase over ~ 1940 –85 (see Figs. 1a and 1b, respectively). Focusing on the 1965–85 time period, which corresponds to peak values of both ASR_HD and AMOC (and also to peak sulfur dioxide emissions from the United States and Europe in CMIP6; Sutton et al. 2018; Dittus et al. 2021), we find that the MMM time-mean anomalies are 1.4 W m^{-2} and 1.0 Sv ($1 \text{ Sv} \equiv 10^6 \text{ m}^3 \text{ s}^{-1}$), respectively. However, when considering the strong and weak subensembles separately we find a large spread in the overall response. For example, strong models have a larger increase in both ASR_HD and AMOC, with 1965–85 mean anomalies of 2.1 W m^{-2} and 1.7 Sv , respectively,

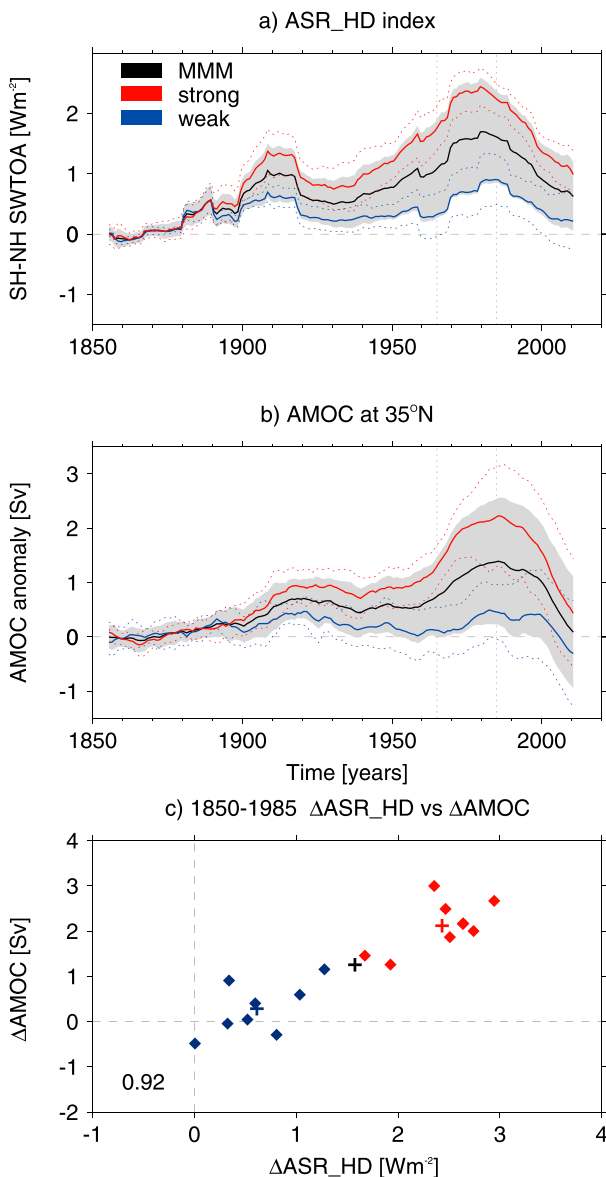


FIG. 1. Simulated interhemispheric imbalance in absorbed solar radiation (ASR_HD) and AMOC. (a) Anomalies of ASR_HD index for the multimodel mean (MMM; black), and for the subensembles for strong and weak aerosol forcing (red and blue, respectively). Thick lines show the ensemble mean and gray shading or dotted lines indicate the 1σ spread. Dashed vertical lines indicate the 1965–85 time period. Anomalies are relative to an 1850–79 climatology. (b) As in (a), but for the AMOC at 35°N. (c) Diamonds show a scatterplot of changes in ASR_HD vs AMOC over 1850–1985 for each model’s ensemble mean. Changes are computed by fitting a linear trend to individual model ensemble-mean time series to compute change per year and then multiplying by the number of years (e.g., 136). Red and blue indicate strong and weak models, respectively. Crosses indicate MMM (black) and strong (red) and weak (blue) subensemble means.

whereas weak models have small, but still statistically significant, anomalies of 0.5 W m^{-2} and 0.2 Sv , respectively. Consistent with Menary et al. (2020), we also find that this relationship applies generally across each model with individual model ensemble-mean trends of ASR_HD and AMOC correlated with a value of 0.92 (see Fig. 1c).

Although the peak values in ASR_HD and AMOC occur in the late twentieth century, we also note that both ASR_HD and AMOC indices increase in the later nineteenth century in the MMM and strong and weak subensembles giving rise to a smaller peak in AMOC at ~ 1920 . This earlier increase is likely to be, in part, related to changes in interhemispheric volcanic forcing [as shown by the spikes in ASR_HD index in Menary et al. (2020)]. However, it is also consistent with the increase in sulfur dioxide emissions over North America and Europe in CMIP6 (Sutton et al. 2018; see Fig. 1c herein) and previous work highlighting the role of AA forcing at this time (Wilcox et al. 2013). As both ASR_HD and AMOC indices appear to diverge between strong and weak models in ~ 1900 , we infer that AA forcing plays an important role in driving AMOC over the whole historical period.

3. Surface density drivers of AMOC

We now turn our attention to changes in surface density flux over the North Atlantic and explore its relationship to AMOC.

Figure 2 shows that for the 1965–85 time mean (i.e., immediately prior to the peak AMOC anomalies) there are significant changes in MMM annual-mean surface heat fluxes (SHF) and precipitation minus evaporation (PmE) fluxes (see Figs. 2a and 2e). Note that we focus on PmE due to its importance in previous studies (e.g., Delworth and Dixon 2006; Menary et al. 2013), and because not all freshwater flux terms were available in all models (not shown). Increased heat loss (negative anomalies) is simulated across much of the higher-latitude North Atlantic, with significant anomalies along the Gulf Stream Extension, in the subpolar North Atlantic (SPNA). Significant changes in PmE are also seen with a reduction over the subpolar North Atlantic and tropical North Atlantic.

However, there are substantial differences between the strong and weak models, especially over the SPNA (cf. Figs. 2b,f with Figs. 2c,g). The difference between the strong and weak ensembles (i.e., strong minus weak) is shown in Figs. 2d and 2h for heat and PmE fluxes, respectively. The comparison shows that the SHF anomalies in the MMM are dominated by the strong models. In contrast, there is relatively little change in SHF in the weak models over much of the North Atlantic, including over the SPNA. For PmE, both strong and weak models show significant changes over many regions of the North Atlantic. In particular, there is a reduction in PmE (negative anomalies) in the subtropics in both strong and weak models that is associated with increased evaporation (not shown). Nevertheless, the difference in PmE anomalies over the SPNA are large, with a significant reduction in PmE only seen in the strong models.

As the differences in surface fluxes are dominated by changes over the SPNA, and as we expect changes in surface

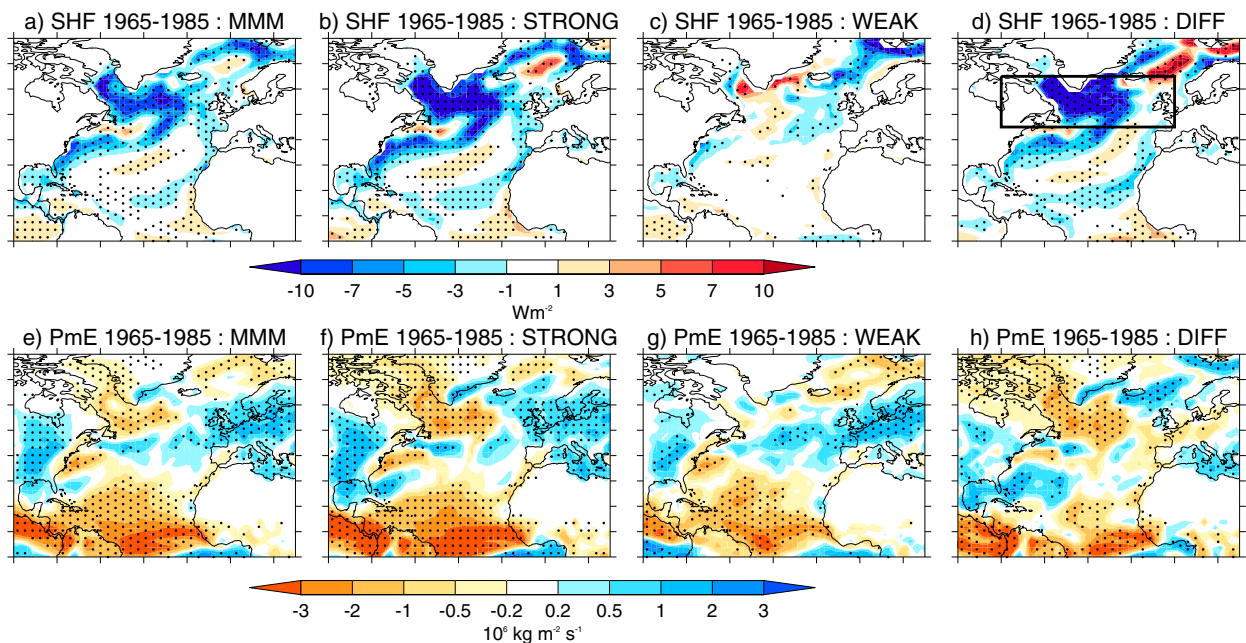


FIG. 2. Comparison of annual-mean surface fluxes anomalies in CMIP6 Historical simulations over the period 1965–85 relative to 1850–1979. (a) MMM anomalies of total surface heat flux (SHF; negative anomalies indicate cooling). (b),(c) As in (a), but for the strong and weak models, respectively. (d) The difference between strong and weak ensembles (i.e., strong *minus* weak). (e)–(h) As in (a)–(d), but for precipitation minus evaporation (PmE; negative is reduced freshwater). For (a)–(c) and (e)–(g) stippling shows where the anomalies are significantly different to climatology at the $p \leq 0.05$ level based on a Student's t test. For (d) and (h) (i.e., the difference) stippling shows where the anomalies of strong and weak are significantly different from each other at the $p \leq 0.05$ level based on a Student's t test. The black box in (d) indicates the region defined as the SPNA (45° – 65° N, 80° – 0° W).

fluxes over the SPNA to drive AMOC (Delworth and Zeng 2016; Xu et al. 2019), we focus on this region for the remainder of this paper. Figure 3 summarizes the time series of changes in SHF (Fig. 3a) and PmE (Fig. 3c) averaged over the SPNA region. Figure 3a shows negative values (i.e., increased heat loss) from ~ 1900 , before a larger decrease from ~ 1940 to ~ 1985 . However, the MMM SHFs are dominated by changes in the strong models over this time period. In contrast, there is a small initial cooling in the weak models in ~ 1900 , but the SHF anomalies diverge between the strong and weak models after this point. PmE also decreases (largely due to increased evaporation) in the MMM after ~ 1900 . However, in contrast to surface heat fluxes, there is little divergence between strong and weak models until after ~ 1940 . Note that the temporal correspondence between SHF and PmE, especially after 1950, suggests that anomalous evaporative cooling is contributing to the SHF anomalies (cf. Figs. 3a and 3c). We will address the overall contributions to SHF in section 4.

Converting the SPNA surface fluxes into surface density flux anomalies shows that SHF dominates the overall surface density flux anomalies, consistent with Hassan et al. (2021) for the MMM (note the difference in y-axis values between Figs. 3b and 3d). The evolution of the thermal surface density flux is also consistent with the evolution of the AMOC over the historical period for the MMM and strong and weak subensembles with the surface heat flux leading AMOC at 35° N by a few years (cf. with Fig. 1b). Indeed, similar to Hassan

et al. (2021), we find a correlation of 0.80 when thermal surface density flux leads AMOC by 4 years (not shown). However, the correlation is 0.92 for the strong models with a lead of 2 years (not shown). Therefore, we conclude that the historical MMM AMOC anomalies in CMIP6 are consistent with the evolution of SPNA surface heat fluxes, and their impact on surface density fluxes, driving the AMOC in the strong models.

4. Decomposing the subpolar North Atlantic surface heat fluxes

The analysis in the previous section showed that SPNA SHF anomalies appear to dominate the evolution of AMOC in the historical simulations, and the differences between strong and weak models. Therefore, in this section we break down the SHF to understand the processes at play.

Figure 4 shows the breakdown of the total annual-mean SHF into the parts associated with turbulent (turHF), surface net shortwave (sNetSW), and surface net longwave (sNetLW) on the top row. When using the MMM, we find that the changes in the sNetSW dominate changes in SHF; the sNetSW is -3.2 W m^{-2} for the 1965–85 mean, and accounts for the majority of the -4.2 W m^{-2} total SHF. In contrast, turHF only accounts for -0.9 W m^{-2} , and sNetLW changes account for a small increase. Hence, the analysis of the MMM is consistent with the hypothesis that AA forcing mainly drives the AMOC

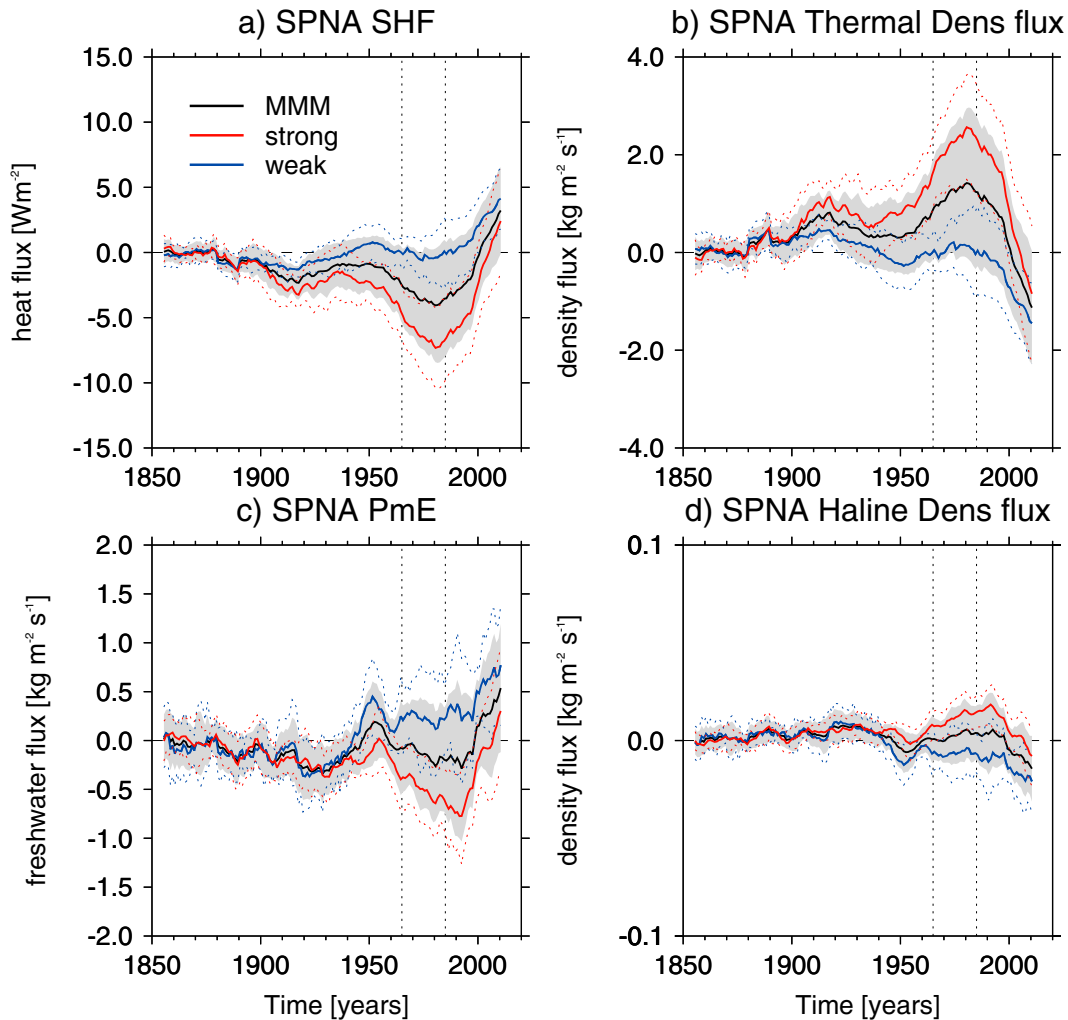


FIG. 3. Comparisons of annual-mean surface heat and freshwater fluxes and equivalent surface density fluxes averaged over the SPNA (45° – 65° N, 80° – 0° W). (a) Total surface heat flux (SHF) and (b) implied density flux due to changes in heat fluxes (10^{-6} $\text{kg m}^{-2} \text{s}^{-1}$); see section 2b for details. (c),(d) As in (a) and (b), but for the precipitation minus evaporation (PmE). Thick lines show the multimodel mean (MMM; black) and strong (red) and weak (blue) subensembles. The 1σ spread of the means is shown in gray shading for the MMM, and with thin dashed red and blue lines for the strong and weak models, respectively. Dashed vertical lines indicate the 1965–85 time period. All time series are smoothed with a 10-yr running mean.

through its direct impact on the SPNA SHF through changes in net solar, as discussed in Hassan et al. (2021).

However, Fig. 4 shows that the divergence in SHF between strong and weak ensembles is *not* driven by changes in sNetSW. Instead, changes in turHF dominate the spread. In terms of the subensemble means, we find that strong models have turHF cooling of -2.5 W m^{-2} by the 1965–85 mean, whereas weak models have a net warming of 1.5 W m^{-2} (i.e., a difference of -4 W m^{-2}). In contrast, the difference between the sNetSW and sNetLW between strong and weak models for the 1965–85 mean is -0.7 and -0.4 W m^{-2} , respectively. The importance of turHF is also evident when we explore linear trends for individual models; the bottom row of Fig. 4 shows that there is a strong relationship between trends

in SHF and AMOC in individual models over 1850–1985 due to the trends in turHF (correlation of -0.92 and -0.82 , respectively). In contrast, the relationship between sNetSW and AMOC is substantially weaker at -0.25 . Note, we also find a correlation of -0.50 between sNetLW and AMOC, but the magnitudes of the sNetLW anomalies are small in comparison. Although we focus on annual-mean SHFs for brevity, we also note that differences in SPNA turHF anomalies are largely dominated by increased winter heat loss due to both sensible and latent heat fluxes, although summer does also play a significant role (see Fig. S1 in the online supplemental material for the seasonal heat flux breakdown).

Alongside the changes in surface heat fluxes, we also find changes in atmospheric circulation. Indeed, Hassan et al. (2021)

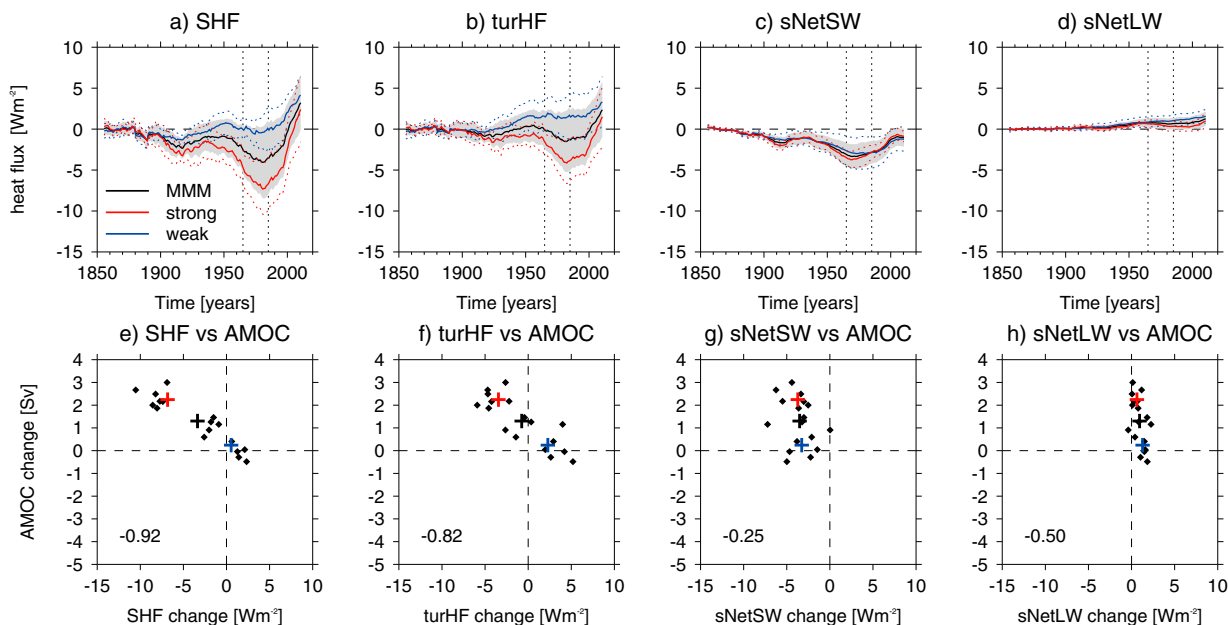


FIG. 4. Time series and trends of annual-mean surface heat flux anomalies averaged over the SPNA. (a) Net surface heat flux anomalies (SHF; W m^{-2}) for the multimodel mean (black) and for the strong and weak subensembles (red and blue, respectively). Gray shading and colored dotted lines show the 1σ ensemble spread. Vertical dotted lines highlight 1965–85; note that this is the same index shown in Fig. 3a. (b)–(d) As in (a), but for the turbulent heat fluxes (turHF), the net surface shortwave (sNetSW), and the net surface longwave (sNetLW), respectively. All anomalies are made relative to the 1850–79 climatology. (e) Scatterplot of linear trends in total heat flux (SHF) compared to trends in AMOC. (f)–(h) As in (e), but for turHF, sNetSW, and sNetLW, respectively. All trends are computed over 1850–1985, and the value shows the total change over that period computed from the linear fit. All time series are smoothed with a 10-yr running mean.

attributed changes in MMM turbulent heat flux anomalies to changes in atmospheric circulation and, specifically, surface wind speed. These changes in annual-mean atmospheric circulation and surface wind (sfcWind) for the MMM ensemble are summarized in Figs. 5a–h for the 1965–85 time period. Note that seasonal changes in atmospheric circulation in summer and winter are similar (not shown). In all seasons, we see an increase in the meridional pressure gradient in the North Atlantic region and, hence, a strengthening of the westerly winds. Again we find that the magnitude of the atmospheric response over the North Atlantic is dominated by the strong models. Therefore, one interpretation is that the larger atmospheric circulation response in strong models is driving the larger response of the AMOC.

However, although they are significant, it is important to note that the changes in atmospheric circulation reported here [and in Hassan et al. (2021)] are relatively small compared to the total variance. For example, the difference in the total change in North Atlantic pressure gradients over 1850–1985 (computed by scaling the linear fit by the total number of years) is only ~ 0.5 hPa between strong and weak for winter means (i.e., where turbulent heat flux anomalies dominate; not shown). Furthermore, turHF values are not just driven by changes in wind speed; contrasts in temperature and humidity at the air–sea interface (i.e., the “thermodynamic” terms) are key drivers of turHF alongside wind speed (see Large and Yeager 2009). We denote these terms ΔT and ΔH , where ΔT is computed as the difference in surface air temperature

and sea surface temperature (e.g., SAT minus SST) and DH is computed as the difference in surface specific humidity (e.g., the CMIP6 variable *huss*) and saturated specific humidity computed from SST (e.g., *huss* minus *satH*), respectively. Exploring these terms further, we find that there are concurrent differences in anomalies of ΔT and ΔH that are consistent with the differences in turHF anomalies seen between strong and weak models (not shown, but see Fig. S1).

To explore the drivers further, we perform a linear decomposition of the turHF and find that the thermodynamic changes are driving both the anomalous turbulent heat fluxes and the difference between strong and weak models. Figure 6 shows a simplified linear decomposition of the annual-mean turHF. Specifically, it shows the multiplication of the air–sea contrasts (e.g., ΔT and ΔH) by sfcWind in order to generate $\Delta T \text{sfcWind}$ and the $\Delta H \text{sfcWind}$ terms and the subsequent linear decomposition terms. In other words, we compute $AB = A'[B] + [A]B' + A'B'$, where A is either ΔT or ΔH , B is sfcWind, a prime (') indicates deviation from the climatology, and square brackets indicate the 1850–79 climatological mean. These terms are computed for each grid point from monthly-mean data before making the annual and spatial averages. The turbulent heat fluxes are proportional to these terms (see, e.g., Large and Yeager 2009), and we find that the SPNA-mean time series correlate highly with the sensible and latent heat flux terms on decadal time scales (see numbers in Figs. 6a and 6d). Figure 6 shows that the evolution of these terms is dominated by the anomalies in the “thermodynamic”

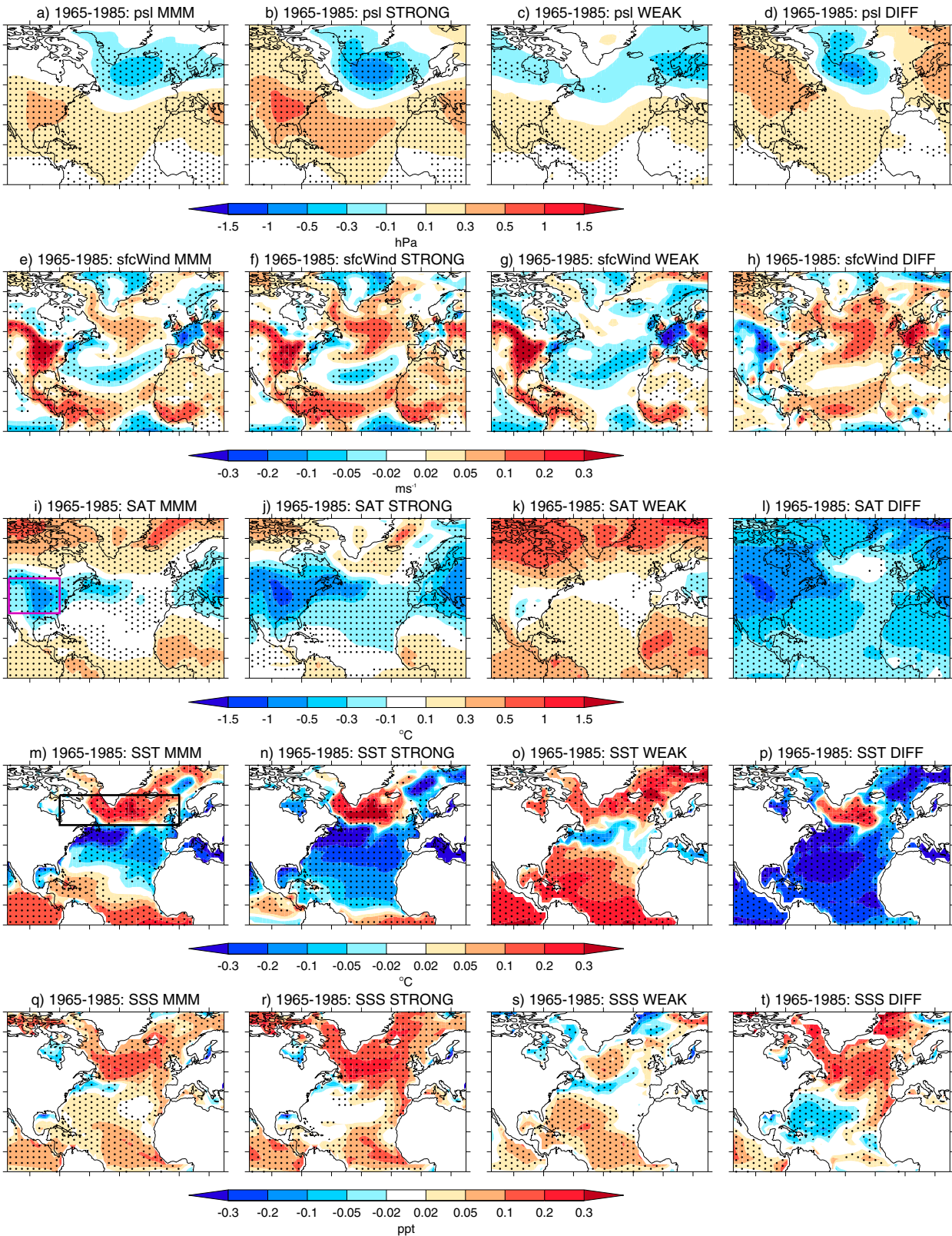


FIG. 5. As in Fig. 2 but for (a)–(d) surface pressure (CMIP6 variable *psl*), (e)–(h) near-surface wind speed (CMIP6 variable *sfcWind*), (i)–(l) surface air temperature (SAT; CMIP6 variable *tas*), (m)–(p) sea surface temperature (SST; CMIP6 variable *tos*), and (q)–(t) sea surface salinity (SSS; CMIP6 variable *sos*).

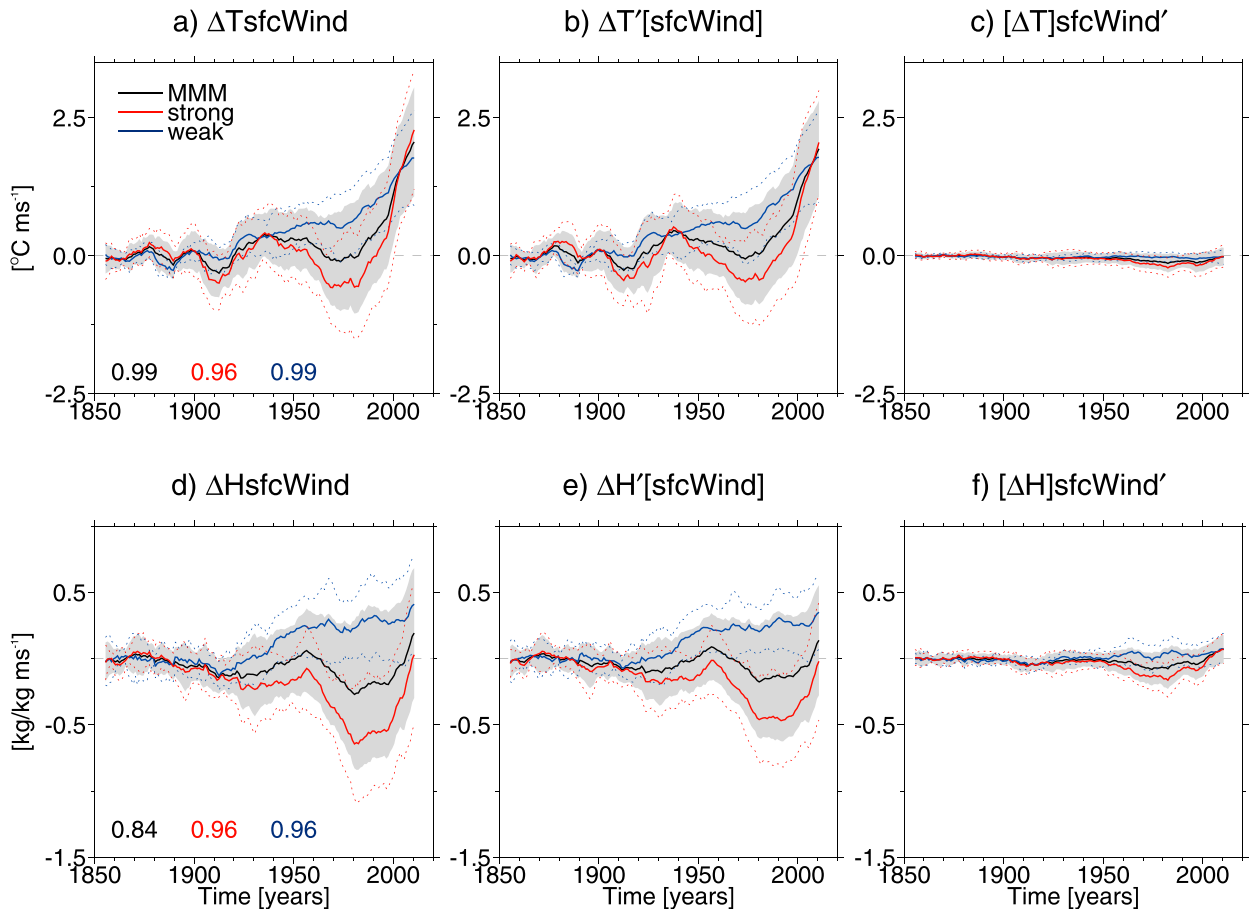


FIG. 6. Linear decomposition of the turbulent heat flux drivers. (a) Anomalies in the air–sea temperature contrast multiplied by surface wind speed anomalies (i.e., $\Delta T_{\text{sfcWind}}$). Numbers inset show the correlation of this term with the sensible heat flux (hfss). (b),(c) Anomalies due to air–sea temperature contrasts ($\Delta T'_{\text{sfcWind}}$) and anomalous wind speed ($[\Delta T]_{\text{sfcWind}}'$), respectively. Here the prime ($'$) indicates anomalies relative to the time-mean climatology and square brackets indicate the time-mean climatology. All climatologies are relative to 1850–79 and time series are smoothed with a 10-yr running mean. (d)–(f) As in (a)–(c), but for the ΔH terms; correlations are with the latent heat terms (hfsls). Note that IPSL-CM6 and NESM3 have been removed from (d)–(f) due to problems with humidity data.

air–sea contrasts [e.g., $\Delta T'_{\text{sfcWind}}$ and $\Delta H'_{\text{sfcWind}}$]; see Figs. 6b and 6e]. In contrast, the role of the anomalous wind anomalies [e.g., $[\Delta T]_{\text{sfcWind}}'$ and $[\Delta H]_{\text{sfcWind}}'$; see Figs. 6c and 6f] is small throughout most of the time period. Note that we do not show the covariance terms (e.g., $A'B'$) as they are small throughout.

5. Continental origin of thermodynamic anomalies?

In the previous section we concluded that increased turbulent heat fluxes in the strong models arise primarily due to increased thermodynamic contrast between the atmosphere and the SPNA. In other words, relative to the sea surface, the atmosphere is colder and drier in models with stronger AA forcing. Figure 7 shows that this cooling and drying of the atmosphere over the SPNA is consistent with the broad impact of external forcing on the interhemispheric difference in surface air temperature and specific humidity (SAT_{HD} and huss_{HD}, respectively; note the HD indicates the hemispheric

difference, which is the Southern Hemisphere mean minus the Northern Hemisphere mean to be consistent with the ASR_{HD} index). The evolution of the SAT_{HD} and huss_{HD} time series is consistent with the evolution of ASR_{HD} index and the AMOC in the MMM, with both indices peaking in the 1965–85 time period (see Fig. 1). However, as with the ASR_{HD} index and the AMOC, MMM anomalies in both SAT_{HD} and huss_{HD} time series are dominated by the strong models and, in contrast, there is relatively little change in the weak ensemble-mean after ~1920. Therefore, the AMOC response appears broadly consistent with the interhemispheric imprint of AA forcing on surface temperature and humidity.

Nonetheless, it is well known that AA forcing is heterogeneous in both time and space (Wang et al. 2015; Lund et al. 2019). Consequently, there are significant regional differences in the pattern of surface forced changes between the strong and weak models. For example, Fig. 5i shows that the largest SAT anomalies in the broader North Atlantic region are

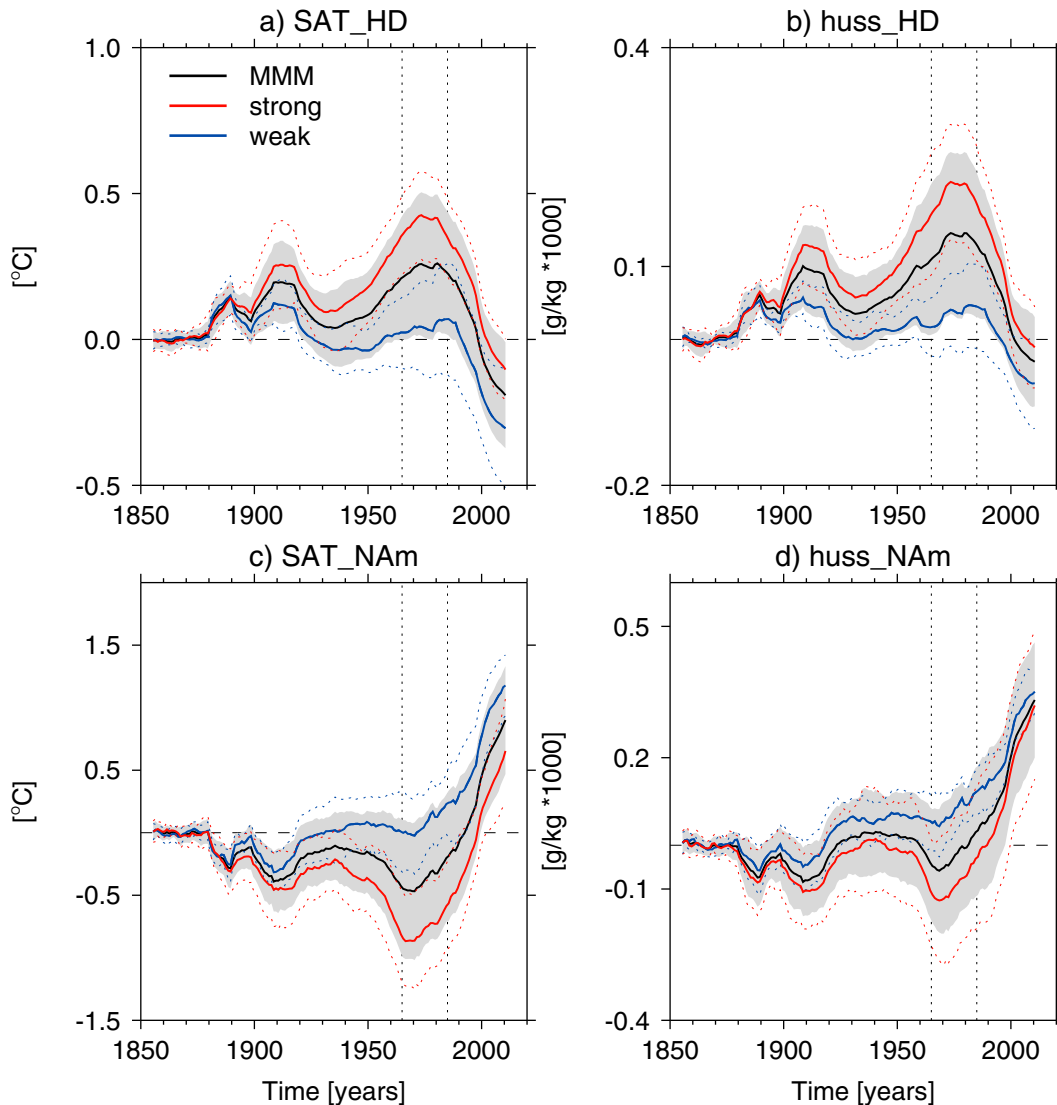


FIG. 7. Key time series of surface temperature and surface humidity. (a),(b) Interhemispheric difference in surface air temperature and surface specific humidity (SAT_HD and huss_HD, respectively). Both are computed as SH minus NH. (c),(d) Surface air temperature and surface specific humidity averaged over the North American continent (SAT_NAm and huss_NAm, respectively; 115° – 80° W, 32.5° – 50° N; see purple box in Fig. 5i). Solid thick lines show the ensemble means for the MMM (black) and the strong (red) and weak (blue) models. The 1σ spread of the MMM is shown in gray shading; thin red and blue dashed lines are for the strong and weak models, respectively. Vertical dashed lines show the period 1965–85. All time series are smoothed with a 10-yr running mean.

located over the North American continent for the 1965–85 mean. Such a cooling of the continental North American region, compared to the ocean, is consistent with the larger changes in net shortwave (see Fig. S2 for global comparison of shortwave and SAT anomalies) as well as the lower heat capacity of the land and other processes that lead to land–sea contrasts in temperatures (Sutton et al. 2007; Joshi et al. 2008).

Focusing on the average of the North American continental region (which we call SAT_NAm), Fig. 7c shows that SAT_NAm cools in the MMM by approximately -0.44°C by

1965–85. However, this cooling is, again, dominated by the strong models, which have a 1965–85 anomaly of -0.89°C , whereas the weak models have a small warming of 0.08°C . This relationship is also clear for individual models, with a correlation of -0.92 between 1850 and 1985 trends in ASR_HD and SAT_NAm (not shown). The cooling is also associated with a drying of the atmosphere in the strong relative to weak models (see Fig. 7d). Note that the largest cooling of the strong models occurs in ~ 1970 , and is broadly consistent with the peak in North American sulfur dioxide emissions that occurred in the 1960s to 1970s (Dittus et al. 2021).

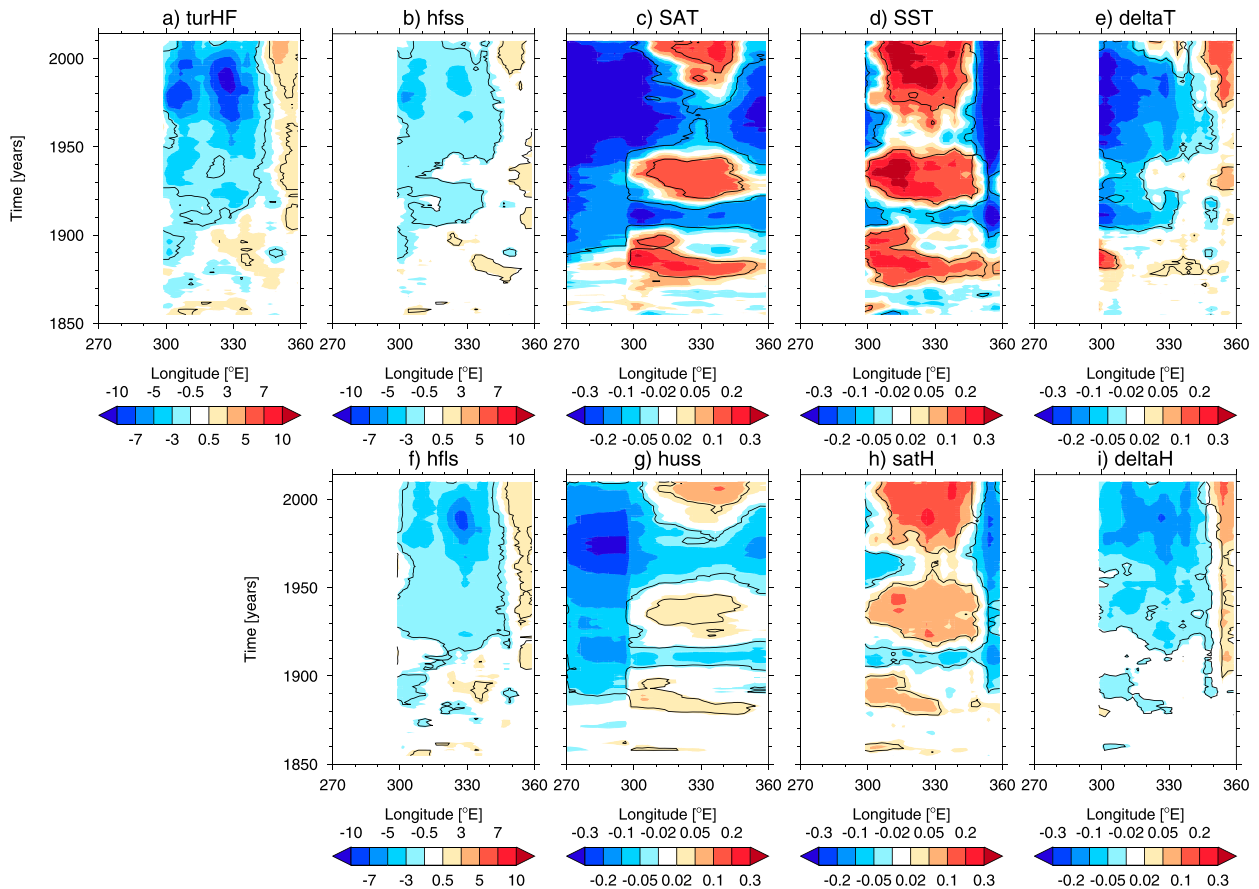


FIG. 8. Longitude–time plots of differences (i.e., strong *minus* weak) in surface heat fluxes and their drivers averaged over the SPNA (50° – 65° N) between 60° and 0° W and atmospheric anomalies over the North American continent (115° – 80° W, 32.5° – 50° N (i.e., the purple box in Fig. 5i). (a) Anomalies in turbulent heat flux (turHF) (W m^{-2}), where negative anomalies are increased cooling of the ocean. (b)–(e) As in (a), but for sensible heat flux (hfss), surface air temperature (SAT), sea surface temperature (SST), and deltaT (e.g., SAT *minus* SST), respectively. (f)–(i) As in (b)–(e), but for latent heat flux (hfls), specific humidity (huss), surface saturated humidity (satH), and DH (e.g., huss *minus* satH). Note that satH is computed as in Eq. (4) from Large and Yeager (2009). Specifically, $\text{satH} = 0.98\rho^{-1}640380 (\text{kg m}^{-1.3})e^{-5107.4\text{SST}}$, where ρ is the density of air and assumed to be 1.22 kg m^{-3} (Large and Yeager 2009). Note that for SAT and huss, values west of 60° W are averaged over the North American continent. Black contours show where the differences are significant at the $p \leq 0.05$ level. Note that IPSL-CM6 and NESM3 have been removed from (f)–(i) due to problems with humidity data.

Therefore, we hypothesize that the regional cooling and drying over the North American continent (which is upwind of the North Atlantic) played an important role in shaping the subsequent evolution of the externally forced AMOC through its impact on the air–sea contrast in temperatures and humidity. In other words, the cool and dry continental anomalies were advected over the North Atlantic, and this drove increased turbulent heat flux cooling of the SPNA. Such a hypothesis is broadly supported by the analysis in Fig. 8, which shows the longitude–time plots of annual-mean differences (i.e., strong *minus* weak) turbulent heat flux anomalies and their drivers. In particular, it is clear from Fig. 8 that the cooling and drying of the atmosphere over the North American continent is substantially larger than the cooling and drying over the SPNA (see Figs. 8c,g). Furthermore, the continental cooling leads the atmospheric cooling over the SPNA, which

is especially clear when comparing the ΔT and ΔH terms (Figs. 8e,i) to SAT and huss (Figs. 8c,g).

Finally, Fig. 8a shows that the anomalous heat fluxes are first seen in the western SPNA, especially in the sensible heat fluxes (hfss; Fig. 8b), and then in the east. This feature is most evident for anomalies in the period ~ 1900 –30, but occurs again from ~ 1940 . The initial anomalies in the west could be consistent with cold advection from the North American continent and the resulting ΔT in particular (i.e., the effect will be largest nearest the source of cold air as the atmospheric anomalies will come into balance with the SST as they are advected over the ocean). The anomalous heat fluxes occurring later in the eastern SPNA after 1940 may be consistent with the intensification of the cold dry signal over North America (i.e., the colder and drier lower atmosphere anomalies advected over the SPNA take longer to come into equilibrium

with the SSTs). However, it may also be consistent with the expected SST warming at this time due to the strengthened AMOC, which can especially impact the eastern SPNA (e.g., Moat et al. 2019).

6. Oceanic feedbacks that act to amplify the AMOC response to anthropogenic aerosols

So far we have explored the forced changes in the AMOC from a surface density flux framework. However, we expect there to be feedbacks that amplify or damp the forced response on the AMOC. For example, through its role in ocean heat transports, an increase in the AMOC is usually associated with a warming of SST (Moat et al. 2019), which will affect the air–sea temperature contrasts and, hence, surface fluxes. Furthermore, transports of heat and salinity/freshwater could impact ocean density (e.g., Menary et al. 2013), which could alter dense water formation (Speer and Tziperman 1992; Petit et al. 2021).

We find that changes in SPNA SST that are due to forced changes in AMOC act as a *positive* feedback on turbulent heat fluxes. Figure 5m shows that for the 1965–85 time period the SPNA is anomalously warm in the MMM compared to the 1850–79 climatology despite the large and consistent cooling of the SPNA (e.g., Fig. 4a), which indicates that the surface warming originates from the ocean rather than the atmosphere. We also find that the SPNA is warmer in strong models than in weak (see Fig. 5p). These changes in SST are consistent with the simulated relationship between SPNA SST and AMOC changes (Menary et al. 2020). As turbulent heat fluxes are proportional to the air–sea temperature and humidity contrasts, and as the warming SST will increase the contrast between the atmosphere and ocean, the simulated warming of the SPNA SST will further enhance the turbulent heat flux cooling in the strong models.

By exploring the role of atmosphere and ocean in driving the air–sea contrasts in temperature and humidity (e.g., ΔT and ΔH), we find that generally the atmosphere is the main driver of the TurHF anomalies. Figure 9 shows the role of the ocean (e.g., SST) and atmosphere (e.g., SAT and huss) in shaping ΔT and ΔH over the SPNA by showing the difference in these terms (i.e., strong *minus* weak). It is clear that the atmosphere plays an important role in ΔT and ΔH ; in particular, negative SAT anomalies contribute to ΔT between ~1900–30 and ~1940–2000 (Fig. 9a), and negative huss anomalies contribute to ΔH after ~1940–90 (Fig. 9b). Furthermore, by comparing the tendency of the smoothed SAT and SST terms, we find periods consistent with the atmosphere driving the ocean between ~1900–15 and ~1940–70 (i.e., the atmosphere is cooling faster; see purple horizontal lines). Therefore, Fig. 9 is consistent with the hypothesis that the SHFs are driving AMOC, and not vice versa.

However, although the SAT anomalies play a pivotal role in driving air–sea contrasts over the SPNA, we also find that SST changes do indeed contribute to broaden and delay the peak in turbulent heat flux cooling. For example, the minima of ΔT and ΔH occur in ~1985, consistent with the peak heat loss in the strong models (e.g., Fig. 4). However, the minima

in SPNA SAT and huss occur earlier, in ~1970. Note that this earlier minimum in atmospheric variables is consistent with the minimum SAT and huss averaged over the North American continent in the strong models (see Figs. 7c,d) and hence is consistent with our hypothesis about the importance of AA-forced continental temperature anomalies and their resultant advection over the North Atlantic. Therefore, SSTs also contribute to the evolution of ΔT and ΔH , and appear important between ~1920 and 1940 and, especially, after ~1960, when SSTs become anomalously warm in the strong models. This warming of SSTs after ~1960 is particularly clear in winter, which is the season with the strongest turbulent heat flux cooling (see Fig. S1). Therefore, the changes in SST in the strong models are clearly acting to increase the differences in surface heat fluxes between strong and weak and to broaden the peak heat flux cooling, especially after ~1980.

The second feedback involves changes in salinity that *positively* feed back onto surface ocean density anomalies. Figure 5q shows that for the 1965–85 time period in the MMM the SPNA is also anomalously salty compared to the 1850–79 climatology. As with other variables, the salinification of the SPNA is dominated by the strong models (Fig. 5r), although there is a small salinification of the weak models (Fig. 5s). When considering the difference between strong and weak models we find that there is a salinification of the SPNA, but a relative freshening of the western subtropical Atlantic (Fig. 5t). These changes in salinity are, again, consistent with the changes in AMOC and its impact on freshwater transports, with increased AMOC leading to increased northward transport of salt (Zhu and Liu 2020).

We find that the changes in SPNA salinity are a key driver of SPNA surface density anomalies. Figure 10 shows surface density anomalies averaged over the SPNA are also very similar to the evolution of the AMOC (see Fig. 1). The MMM index shows an increase in surface density from ~1880 to ~1910 before decreasing slightly and leveling off until ~1960 and increasing up to ~1980. However, the MMM is again dominated by the strong models after ~1900. By decomposing the surface density changes into both the part due to changes in surface salinity and surface temperatures (RhoS and RhoT respectively; see section 2b for details of computation), we find that the long-term increase in surface density is dominated by changes in salinity (i.e., RhoS) in the strong models. Salinity also contributes to the increase in SPNA density up to ~1910 in both strong and weak models.

In contrast, RhoT appears to contribute little to the overall changes in surface density until after 1970, when SPNA warming causes a relatively fast decline in SPNA surface density anomalies. Note that this result is in contrast to Hassan et al. (2021), who argued that SST changes dominated surface density, and suggests that their analysis is dominated by the decreasing AMOC (and related RhoT changes) after 1980. However, we also note there are small but significant positive RhoT anomalies in ~1900–10 and in ~1950–80 in the strong models. These are both periods of large deviations in ΔT (see Fig. 9) and SHF between strong and weak (see Fig. 4), suggesting that AA-driven atmospheric cooling did contribute to the surface SPNA density anomalies in these time periods.

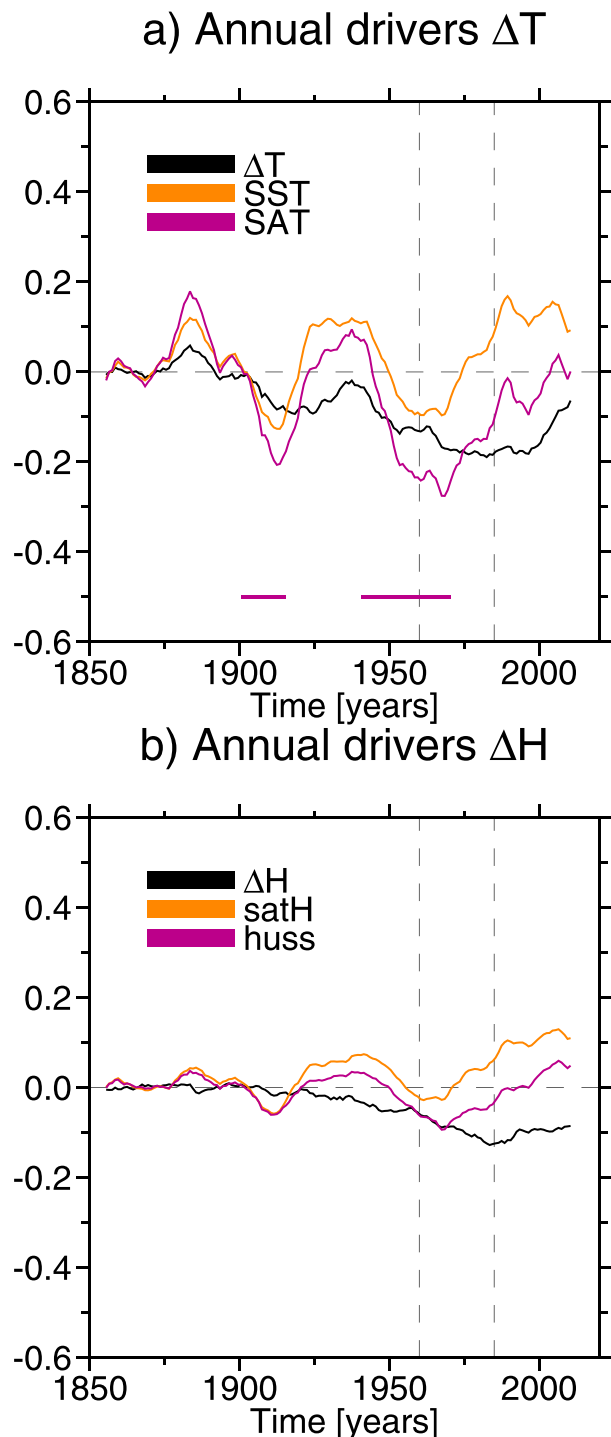


FIG. 9. Atmospheric and oceanic contributions to air–sea contrasts in temperature and humidity (e.g., ΔT and ΔH) averaged over the SPNA (50° – 65° N, 70° – 0° W; note the smaller latitudinal area chosen to represent the region of positive SST anomalies in Fig. 5). (a) The difference in annual-mean ΔT (e.g., SAT minus SST (black), SST (orange), and SAT (purple) between the strong and weak ensembles (e.g., strong minus weak). (b) As in (a), but for ΔH (e.g., huss minus satH), surface specific humidity (huss), and saturated humidity (satH) computed from SST;

However, it is clear that the overall influence of SST on ocean surface density trends was small.

At first glance, these changes in surface density due to salinity are consistent with previous work that explore the impact of AA on AMOC via analysis of surface density anomalies (e.g., Delworth and Dixon 2006; Menary et al. 2013). However, we argue that these salinity-driven surface density anomalies are primarily a feedback onto AMOC and not an initial driver of the AMOC. For example, PmE only diverges between strong and weak after ~ 1940 (see Fig. 3), but surface density diverges around ~ 1900 . Furthermore, we also find that the initial divergence in surface density appears to be due to surface temperature, whereas the surface density anomaly due to salinity only diverges at about ~ 1915 (see Fig. 10). Similarly, lagged correlations computed using the whole time series 1850–2014 show that the maximum correlation is found when AMOC leads the surface density anomalies due to salinity by a few years (not shown). For models where data are available, we also find that ocean freshwater flux divergence anomalies dominate the full-depth salinity budget in the SPNA and that the freshwater flux divergence in strong and weak models diverge in ~ 1900 , consistent with changes in the AMOC (not shown).

7. Discussion

a. Summary of the proposed mechanism

As already shown by Menary et al. (2020), the evolution of externally forced changes in the AMOC in historical simulations made for CMIP6 is highly dependent on the strength of the AA forcing/climate system response to AA forcing. Here we have shown that the spread in the model AMOC response appears to be mainly related to the strength of anomalous turbulent heat flux cooling over the SPNA, which is, in turn, related to the fact that the atmosphere is anomalously cooler and drier in models with strong AA forcing. We hypothesize that this difference in turbulent heat flux cooling is largely a result of the differences in local cooling over the continents, and specifically the North American continent. Nevertheless, we emphasize that this mechanism is in addition to the more “direct” impact of changes in downwelling SW over the SPNA. In so-called weak models, the negative anomalies in netSW over the SPNA clearly counteract positive turHF anomalies (see Fig. 4), therefore likely delaying a reduction in AMOC. However, this direct impact on the SPNA heat budget does not explain the difference between strong and weak models, as shown by the lack of correlation in Fig. 4g.

←

$\text{satH} = 0.98\rho^{-1}640380(\text{kg m}^{-3})e^{-5107.4/\text{SST}}$, where ρ is the density of air and assumed to be 1.22 kg m^{-3} (Large and Yeager 2009). Note that IPSL-CM6 and NESM3 have been removed from (b) due to problems with humidity data. Purple horizontal bars in (a) approximately indicate where the negative tendency in SAT is larger than for SST, and thus where the atmosphere is driving the ocean rather than the other way round.

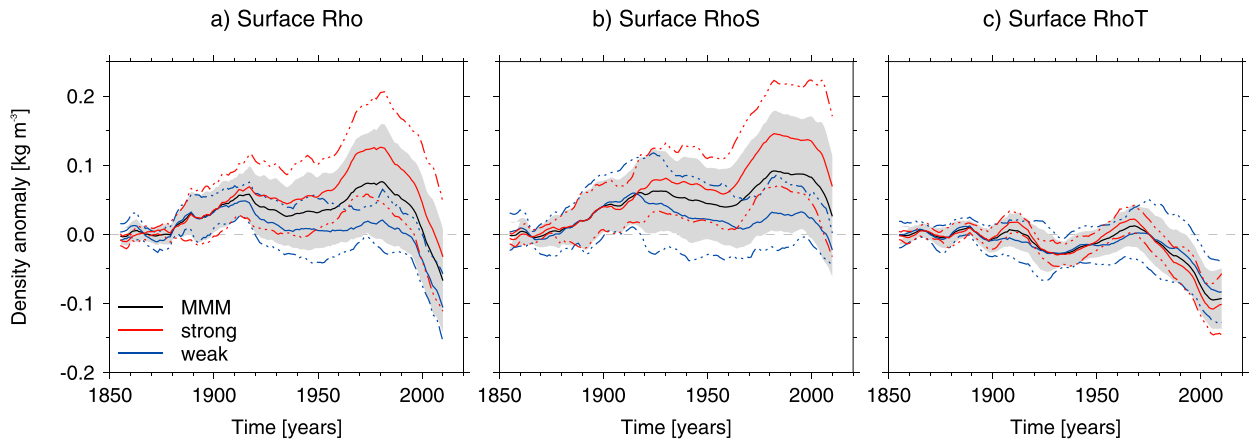


FIG. 10. Evolution of SPNA annual-mean surface density anomalies in CMIP6 historical simulations, and the role of salinity and temperature. (a) Surface density anomalies in CMIP6 MMM (black), and strong (red) and weak (blue) subensembles. Gray shading and thin colored lines show the $\pm 1\sigma$ spread. (b) As in (a), but for the contribution of salinity, e.g., by using climatological SST (see text for details). (c) As in (b), but for the role of temperature by using climatological SSS. All time series are smoothed with a 10-yr running mean.

The hypothesized mechanism to explain the difference in strong and weak is summarized in the schematic shown in Fig. 11 and progresses as follows. First, increased aerosol and aerosol precursor emissions drive negative radiative forcing over the North American continent. The AA forcing leads to the rapid onset of cold and dry surface anomalies over land relative to the ocean (Fig. 7c). These cold and dry anomalies are then advected across the North Atlantic Ocean (likely by the climatological winds) and lead to increased air–sea temperature and humidity contrasts and, hence, increased SHF cooling of the SPNA due to turHF (Fig. 6). The increased SHF cooling drives increased transformation of surface water due to increased surface density flux (Fig. 3) and, subsequently, a strengthening of the AMOC.

The strengthening of the AMOC also feeds back onto itself positively due to related changes in ocean heat and salt transports. In particular, increased ocean heat transport warms the SPNA SST, which further amplifies air–sea contrasts in temperature and humidity and, hence, turbulent heat fluxes. The SST feedback broadens and delays the peak SHF cooling of the SPNA and, potentially, the AMOC strengthening. Increased salt (or reduced freshwater) transport also causes a salinification of the SPNA, which leads to increased surface density. In the framework of surface water mass transformation (Walsh 1982), increased surface density would increase the outcropping area of isopycnals in winter associated with the lower limb of the AMOC that can be transformed by the surface fluxes (Petit et al. 2021).

b. Constraining the historically forced AMOC changes

So far we have shown that the evolution of externally forced AMOC variability in CMIP6 historical simulations over 1850–1985 shows a wide spread that is related to strength of the AA forcing. Therefore, we now address whether we can constrain the historically forced AMOC response by comparing the simulation of key variables against observations. Specifically, we compare SPNA surface properties and surface

temperatures over the North American continent and over the Northern Hemisphere. We do this by computing linear trends from all individual ensemble members and compare them with contemporaneous trends from the observations. Due to the lack of SPNA data over 1850–1900, we focus on trends over 1900–85.

As in Menary et al. (2020), we find that SPNA SST is a weak constraint on the externally forced AMOC response. Figure 12a shows that the MMM SPNA SST shows noticeable variability throughout the historical period, with a warming peak at ~ 1930 , a minimum at ~ 1970 , and a warming after ~ 1985 . However, there is little difference in the strong and weak models ensemble-mean overall evolution, although strong models show slightly colder anomalies in ~ 1910 and ~ 1970 , consistent with increased surface flux cooling in these time periods (e.g., Fig. 9). However, it is clear that the ensemble-mean temperature anomalies (i.e., the externally forced response) are small in terms of long-term trends and also small compared to observed or simulated multidecadal variability. Therefore, when computing trends of the SPNA SST (i.e., Fig. 12e) the observed trend falls within the 5%–95% confidence interval of nearly all models.

SPNA SSS increases in the historical period up to ~ 1980 in the strong models, and these changes appear inconsistent with observations. Figure 12b shows the time series of SSS. In the strong models, SPNA surface salinity increases from 1850, but with a more rapid increase between 1950 and 1985 largely in response to the simulated AMOC increase. In comparison, weak models show a smaller increase from 1850 to 1910, but then show little trend thereafter. However, in contrast, observations show a reduction in SPNA surface salinity over the historical period, and especially following the 1960s, the well-known Great Salinity Anomaly (Dickson et al. 1988). When we compare trends between the models and observations in Fig. 12f, we find that the observed trend is more consistent with weak models. The observed trend falls outside the 5%–95% confidence interval for the

Hypothesized mechanism for the AMOC response to anthropogenic aerosol

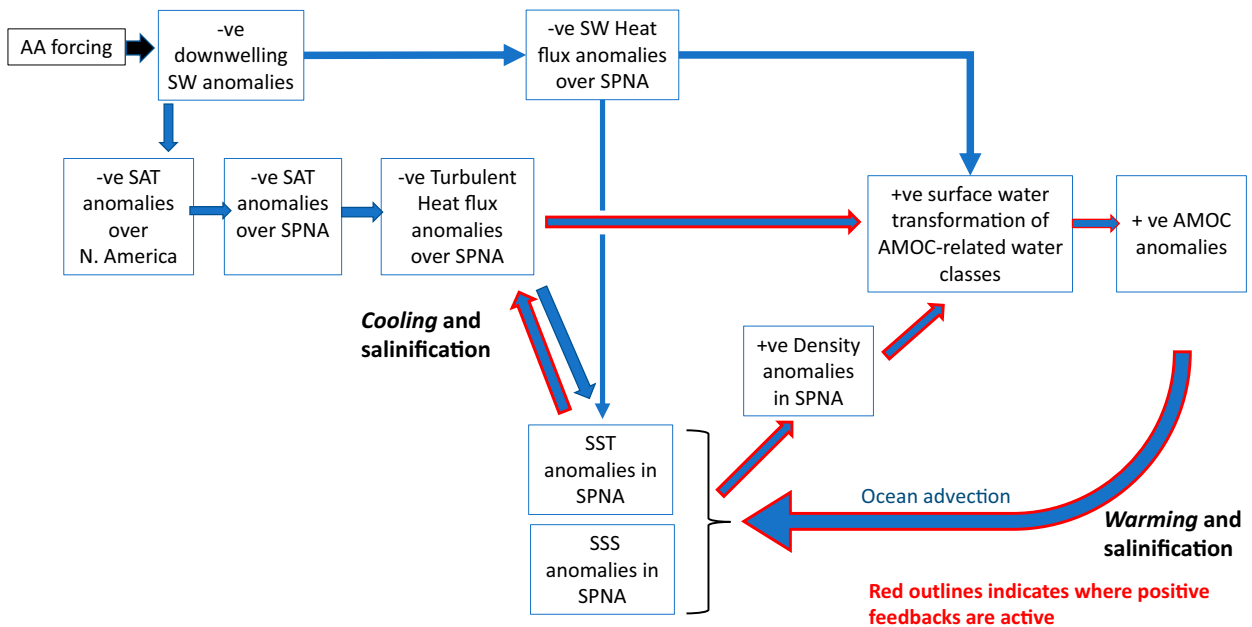


FIG. 11. Schematic of proposed mechanism explaining the response of AMOC to anthropogenic aerosol forcing in CMIP6 historical simulations on decadal time scales. Arrows with red outlines indicate pathways where positive feedbacks are active, e.g., on SPNA density through salinity advection, or through the impact of SPNA SSTs on turbulent heat fluxes. Negative heat flux anomalies indicate increased cooling of the ocean. Note that although downwelling SW anomalies also impact SST anomalies in the SPNA, we have shown that this process does not dominate SPNA heat budget on these time scales (i.e., 1850–1985); hence, we show this link as a thinner arrow. Also note that, for simplicity, we only show one arrow representing oceanic heat and freshwater transport, but we acknowledge that these are not necessarily in phase at all time scales and that such differences could be important in shaping the response.

majority of strong models (7 of 9) but is within the majority of weak models.

We also find that the simulated changes in surface temperatures in the strong models are not consistent with observations. Figure 12c shows that North American continental surface air temperature (i.e., SAT_NAm) cools in the MMM, largely due to the substantial cooling in the strong models. However, we find that the observed continental surface temperature warms almost continuously over the historical period following ~1890. There is a small observed cooling over ~1940–70, but this cooling is substantially smaller than is simulated in the strong model ensemble mean. When comparing the 1900–85 trends in SAT_NAm in Fig. 12g we find that the observed trend is not consistent with the strong models (the trend is outside the 5%–95% confidence interval for 8 out of 9 of the strong models) but is consistent with all the weak models. Furthermore, Fig. 12d shows that there is also only a small warming in Northern Hemisphere surface temperatures (ST_NH) before ~1985 in the MMM, which is again dominated by no net warming in the strong models and a hemispheric cooling circa 1950–75. However, in contrast, the observed Northern Hemisphere generally warms apart from ~1940–70, but this cooling is again substantially smaller than in the strong model ensemble mean. When comparing the 1900–85 trends in ST_NH in Fig. 12h we find that the observed trend is not consistent with the strong models (the

trend is outside the 5%–95% confidence interval of trends in all strong models), but it is consistent with most of the weak models (5 out of 8). Therefore, we infer that the anomalous turbulent heat flux anomalies, which are driven by the cooling atmosphere, are very likely to be overestimated within the strong models.

Taken together, the evidence presented here suggests that the magnitude of the historical externally forced AMOC strengthening in the strong CMIP6 models is not consistent with observations. In particular, we show clearly that the simulation of North American surface air temperatures and Northern Hemisphere surface temperatures are not consistent with observations in the strong models (see Fig. 12c). As these are key regions affected by AA forcing, we conclude that the AA forcing, or the response to AA forcing, is too large in the strong models. Such a conclusion is consistent with a number of studies that document a too large AA-driven cooling in CMIP6 historical simulations (Flynn and Mauritsen 2020; Dittus et al. 2020; Wang et al. 2021; Zhang et al. 2021). As there is a strong relationship between the strength of the AA forcing/response and the changes of the AMOC in CMIP6-class models (i.e., Fig. 1), it follows that the AMOC response is overestimated too, irrespective of the exact mechanism. This conclusion is also supported overall by the comparison of simulated SPNA salinity with observations, which indicates that the SPNA salinity increases too

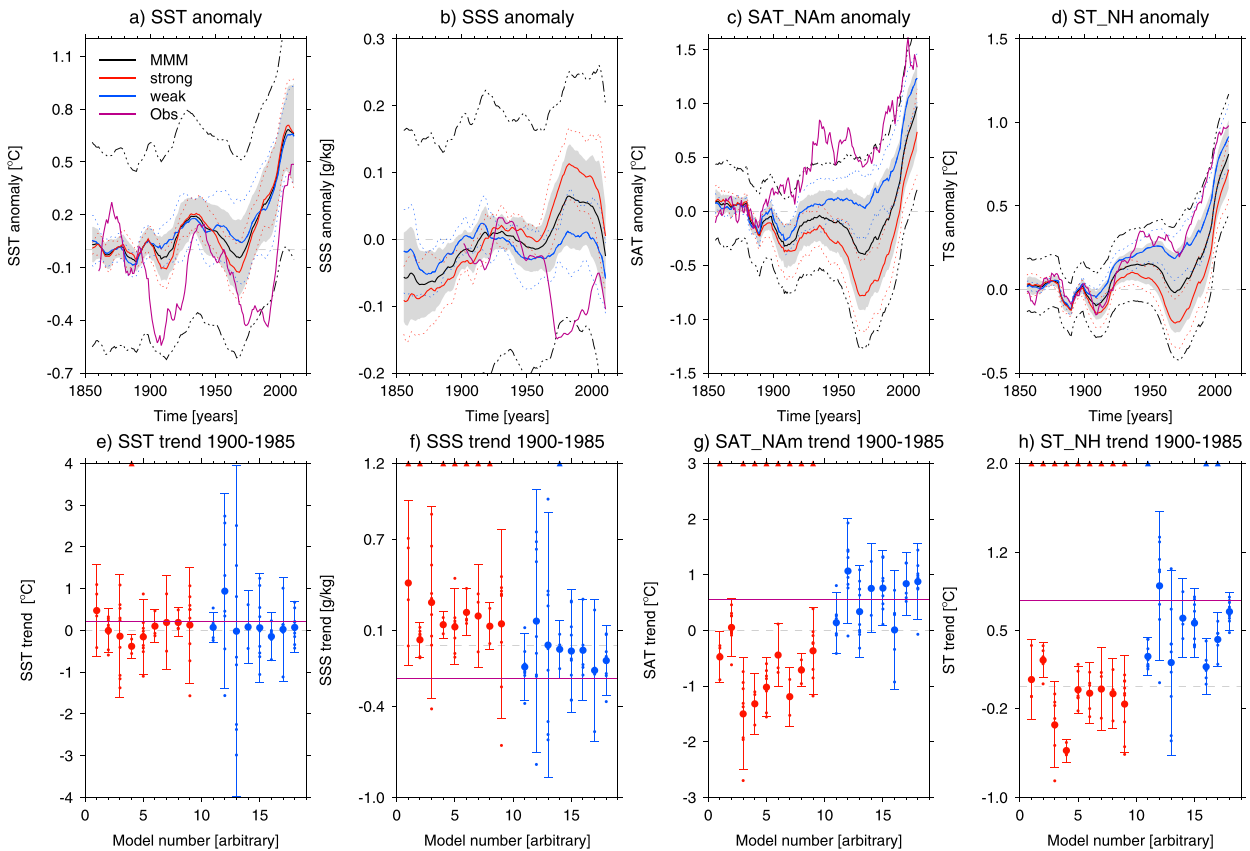


FIG. 12. Comparison of historical simulations with observations for key metrics. (a) Anomalies for SPNA sea surface temperature (SST) relative to 1850–99, for the MMM (black), strong (red) and weak (blue) ensembles, and observations (purple; ERSSTv5). The 1σ spread of the individual model’s ensemble means is shown by the black shading or red and dotted lines for MMM and strong and weak models respectively. The black dot-dashed line shows the 5%–95% confidence interval of the MMM ensemble mean based on all the individual members. (b)–(d) As in (a), but for SPNA sea surface salinity (SSS), North American surface air temperature (SAT_NAm), and Northern Hemisphere surface temperature (ST_NH; e.g., SAT and SST combined and averaged over 0° – 60° N), respectively. Observations are given by the “annually binned sea surface salinity” dataset from Reverdin et al. (2019) for (b), and BEST for (c) and (d). Note that anomalies for SSS are computed over 1900–50 due to shorter observations. Note also that (c) shows the same time series as shown in Fig. 7c, but now for the 1850–1900 climatological period. (e) Comparison of observed and simulated linear trends of SPNA SST computed over 1900–85 for each member, and the large dot shows the ensemble mean for each model). Error bars show the 5%–95% confidence interval for the model ensemble means computed by using the individual model members. Horizontal purple line shows the observed trend computed over the same time period. Triangles at the top of the plot shows where observations are outside the 5%–95% confidence interval. (f)–(h) As in (e), but for SSS, SAT_NAm, and TS_NH, respectively.

much in the strong models, which appears consistent with a too large AMOC increase.

c. Wider implications and caveats

In this paper we have tried to present a broad and in-depth analysis of the role of AA forcing in driving the AMOC in CMIP6 historical simulations. The analysis presented here raises a range of questions that will need to be addressed in future research. In particular, questions remain regarding the exact role of the positive feedbacks outlined in section 6, the role of the atmosphere in driving SHF anomalies, the regions most important for mediating the AA-driven AMOC response, and the wider implications.

Although positive feedbacks appear in operation in the simulated evolution of the externally forced AMOC, their

relative importance remains unclear. For example, to what extent does the positive feedback on heat fluxes contribute to the increasing AMOC? Furthermore, how important are the salinity-driven surface density changes, which have been the focus of previous studies (e.g., Menary et al. 2013), compared to the AA-driven SHF anomalies? It is also important to emphasize that the feedbacks discussed in section 6 are always positive *only* in the presence of continued externally forced cooling of the SPNA due to AA forcing. Otherwise, the role of ocean heat transports and the subsequent SPNA warming could dominate density anomalies and contribute to a reduction in SPNA surface density. Indeed, such a temperature-driven negative feedback may be a key driver of the decreasing AMOC in strong models after ~ 1985 , but more work is needed to understand this time period, which is complicated

by large GHG-forced changes (Menary et al. 2020). Future work could address these questions through computation of surface water mass transformations across the SPNA in models in order to understand the relative role of surface density fluxes as opposed to surface density anomalies in driving anomalous transformations [i.e., as in Petit et al. (2021)] or to focus on the importance of different regions (e.g., Yeager et al. 2021). Given the importance of salinity highlighted here, further detailed analysis and budgets are also necessary to understand the key drivers of the SPNA salinity changes in strong models. However, many of the important variables related to freshwater budgets (particularly those related to sea ice) were not available for analysis across all models, and full-depth ocean transports may not be sufficient. Therefore, further careful computation of freshwater transports to focus on the upper ocean is needed.

Despite a significant atmospheric circulation response in the historical simulations related to AA forcing (e.g., Fig. 5), the AMOC mechanism presented here is essentially a thermodynamically driven mechanism. In other words, changes in the atmospheric circulation strength play little role in explaining the difference in AMOC evolution between strong and weak models. However, the ΔT anomalies could, in part, be related to changes in surface atmospheric temperature associated with changes in atmospheric circulation (e.g., a shift in the jet position; Ma et al. 2020), which we have not explored here. Therefore, further analysis of the forced response in atmospheric circulation is needed, not least to understand the mechanistic origin of the response and its realism. It is also important to emphasize that models have known deficiencies in simulating the atmospheric circulation response to a range of drivers, including external forcing—the signal-to-noise problem (Scaife and Smith 2018). Therefore, the extent by which AA forcing drove the AMOC in the real world is still unclear as we cannot trust that the atmospheric circulation response is adequately represented.

We also recognize that the hypothesis that North American continental region is the key region for mediating the AMOC response to AA in the strong models is also uncertain. This is because AA forcing is the ultimate driver of a range of climate signals in the strong models (e.g., surface radiation budgets and surface temperature over the Northern Hemisphere; see Fig. S2). Furthermore, the AMOC and climate-related feedbacks described above and other confounding factors (e.g., contemporaneous external forcing) make it more difficult to ascribe causality. In particular, the role of volcanic forcing has also not been assessed here, and natural forcings do contribute to AMOC variability in CMIP6 historical simulations Menary et al. (2020). Changes in land surface use can also be an important driver of North American continental surface temperatures (Andrews et al. 2017) and could thus contribute to the differences between models via the proposed mechanism here. However, initial analysis of fixed land use simulations made with UKESM1-0-LL as part of the Land Use Model Intercomparison Project (LUMIP; see Lawrence et al. 2016) suggests a relatively small impact on ASR_{HD} (not shown) and, we assume, AMOC, but further analysis is needed. Nevertheless, this range of uncertainties

highlights the difficulty in fully unraveling the full mechanism using only diagnostic analysis of historical simulations. Therefore, the importance of AA forcing in different regions and the processes that mediate the AMOC response still need to be tested through further targeted experiments (e.g., by introducing idealized regional downwelling shortwave anomalies). Future work could also examine the importance of continental surface air temperature responses in mediating the AMOC response to other forcings such as volcanoes etc.

The results also raise a number of additional questions that need further investigation. For example, it is not clear if the mismatch between the evolution of historical AMOC in MMM CMIP6 simulations and that interpreted through indirect measurements (e.g., Caesar et al. 2018, 2021) is explained by the too large AMOC response in the strong models. Therefore, questions still remain about how models represent the evolution of AMOC over the historical period. There are also questions about what these results mean for future AMOC changes. For example, Weijer et al. (2020) showed that the rate of AMOC decline in CMIP6 projections is model dependent. Given the large reduction in AMOC in strong models after ~1985 (see Fig. 1) it is plausible that some of this difference is related to the too large historical AMOC changes in strong models and the sensitivity to AA forcing, but it is unclear if this is the case. It is also not clear what aspects of the AA forcing and climate response is leading to the large ASR_{HD} and AMOC response in the strong models, or whether the processes are the same in all time periods. Indeed, there is still large uncertainty in the models' effective radiative forcing and the spatial distribution of forcing (Smith et al. 2021). Furthermore, Weijer et al. (2020) and Menary et al. (2020) both show a correlation between models with a strong transient climate response (TCR) and historical AMOC trends (i.e., models with a larger AMOC trend have a larger TCR). Therefore, it is likely that both the time-varying instantaneous AA radiative forcing and the range of climate adjustments and feedbacks (including temperature-related feedbacks) are important for shaping the overall response of AMOC to AA forcing. Hence, future work is needed to better constrain the response of the climate system to AA forcing and to understand the ASR_{HD} and AMOC relationship in different time periods. However, for now, it is crucial that research reflects the diversity, and uncertainty, in the AA forcing and response rather than focusing on the MMM.

We should also note briefly that there are also inevitably caveats to the analysis presented here. For example, we have not included all CMIP6 models, which reflects the need for multiple variables and ensemble members. Therefore, we chose to focus on a smaller ensemble of models where we have complete datasets for at least three members. However, Menary et al. (2020) have already shown that the relationship between ASR_{HD} and AMOC holds in a larger range of CMIP5 and CMIP6 models and we assume that our results will broadly hold across other models. Nevertheless, the exact details of the mechanism will likely differ from model to model due to model differences. The limited number of ensemble members will also inevitably lead to some uncertainties for model-dependent

results (Tandon and Kushner 2015). Although we mitigate this sampling uncertainty through the creation of the strong and weak subensembles, we note that the representation of internal variability remains another key uncertainty in understanding AMOC variability and its impact (Yan et al. 2018; Bonnet et al. 2021; Jackson et al. 2022).

One aspect that needs further exploring is the exact role of sea ice in mediating the response of SPNA heat fluxes to AA forcing. Indeed, sea ice grows in the strong models [not shown, but see Robson et al. (2020) for analysis of UKESM1-0-LL] and so questions arise about how this affects heat and freshwater fluxes and SHF in the SPNA and Arctic (which can also be important for AMOC; Sévellec et al. 2017; Zhang and Thomas 2021). Sea ice can also be heavily biased, which affects the relationship with SPNA SHFs (not shown); for this reason we chose not to include CanESM5 in the analysis due to a large positive sea ice bias in the western SPNA (Swart et al. 2019).

8. Conclusions

We have analyzed CMIP6 historical simulations in order to understand the processes leading to the anthropogenic aerosol (AA)-forced increase in Atlantic meridional overturning circulation (AMOC) over the period 1850–1985 shown in Menary et al. (2020). We explore ensemble-mean changes in AMOC between models, and using an interhemispheric proxy of AA forcing response we split models between “strong” or “weak” AA forcing. The key results are as follows.

- There is a large spread in the simulated AMOC changes in CMIP6 historical simulations that is related to the spread in the strength of the AA forcing response. In particular, the multimodel mean (MMM) response is dominated by anomalous AMOC in the strong models. In contrast, the weak models show little change in AMOC.
- Surface density fluxes due to surface heat flux (SHF) cooling and resultant surface density fluxes over the subpolar North Atlantic (SPNA; 45°–65°N) appear to dominate the simulated increase in AMOC in strong models over 1850–1985 [consistent with Hassan et al. (2021), who found a similar relationship over 1940–2014 for the MMM].
- Differences in downwelling shortwave radiation over the SPNA do not explain the difference between net SHF over the SPNA or the evolution of AMOC in models. Instead, turbulent heat fluxes dominate the spread in AMOC responses. Hence, AA forcing does not act directly on the AMOC through only changes in the radiation balance over the SPNA.
- The anomalies in annual-mean turbulent heat flux appear to be dominated by changes in temperature and humidity across the air–sea interface (ΔT and ΔH , respectively), rather than changes in wind speed. Therefore, AMOC is primarily driven by a colder and drier atmosphere in the strong models compared to the weak ones.
- The colder and drier atmosphere is consistent with larger AA-forced changes in downwelling shortwave and, hence, colder and drier temperatures over the continental regions, especially over North America. Hence, the increase in

AMOC appears consistent with the advection of cold and dry air from the continents over the ocean, which drives increased turbulent heat fluxes through increased air–sea contrasts.

- AMOC-related changes in ocean salinity and surface temperatures in the SPNA act to amplify the AMOC increase. Specifically, the increase in AMOC leads to a saltier SPNA that increases surface density anomalies. Additionally, despite the strong SHF cooling in the strong models, the SPNA warms in response to the strengthened AMOC. This warming acts as a positive feedback on the SHF cooling and surface density flux by increasing the air–sea temperature and humidity contrasts. However, it is less clear if this SHF feedback affects the AMOC.
- The evolution of surface temperature over North America and the Northern Hemisphere in strong models over 1900–85 is not consistent with observations. Furthermore, strong models also simulate the wrong sign of SPNA surface salinity trends. Therefore, comparisons with observations suggest that the AMOC increase in the strong models is likely to be overestimated.

In this paper we have highlighted the uncertainty in the historically forced AMOC response in CMIP6 models, and its dependence on the uncertainty in AA forcing. We have presented the surprising findings that diversity in AA-forced AMOC change is explained by the spread in turbulent heat flux anomalies over the SPNA (rather than the changes in downwelling shortwave), and that the AA-driven cooling over the continental regions mediates the AMOC response to AA forcing. In all models, AA forcing drives the AMOC directly by changing the radiation budget over the North Atlantic, but in strong models the indirect effect of AA forcing on AMOC, through its impact on atmospheric temperature and humidity, is at least as important. Furthermore, we provide evidence that this indirect “thermodynamically” driven mechanism, and hence the increase in the externally forced AMOC change, is likely too large in the strong models and thus in the CMIP6 MMM.

Given the uncertainty in AA forcing, and the AMOC response to it, care is needed in using and interpreting simulated changes in the North Atlantic in CMIP6 historical runs. More research is needed to understand the wider implications of the spread in historical AMOC responses, including the potential impact on future projections and in constraining past changes. Further research is also needed to understand if the mechanisms presented here can be generalized to other forcings (e.g., volcanic) and other time periods as well as to understand the relevance to the real world. Indeed, the uncertainties in the external forcing and the simulated response in the ocean and atmosphere make it difficult to attribute past AMOC changes based on CMIP6 models alone.

To make progress it is crucial to minimize the uncertainty in historical aerosol forcing and how the climate system responds to those changes. It is also important to better understand the representation and drivers of AMOC and how the ocean and atmosphere responds to different external forcing in models (including the signal-to-noise problems; Scaife and

Smith 2018) and in the real world. Note that we were only able to discern the role of turbulent heat fluxes and continental temperature anomalies in CMIP6 models by contrasting models with strong and weak AMOC responses. Therefore, these results highlight the continuing need to understand the range of model responses and mechanisms to AA forcing, and not just focus on one model or the multimodel mean.

Acknowledgments. We thank John Fasullo and two anonymous reviewers for their thoughtful comments that improved the clarity of the manuscript. This study was funded by the NERC ACSIS program (NE/N018001/1 and NE/N018044/1). JR was additionally funded by NERC via NCAS, as well as the WISHBONE (NE/T013516/1) and SNAP-DRAGON (NE/T013494/1) projects. CJ was funded by the NERC UKESM program (NE/N017978/1). We acknowledge the World Climate Research Programme, which, through its Working Group on Coupled Modelling, coordinated and promoted CMIP6. We thank the climate modeling groups for producing and making available their model output, the Earth System Grid Federation (ESGF) for archiving the data and providing access, and the multiple funding agencies who support CMIP6 and ESGF. This work used JASMIN, the U.K. collaborative data analysis facility, and model data were analyzed with CDO (Schulzweida 2021).

Data availability statement. The CMIP6 model data used in this study were downloaded from the ESGF (e.g., <https://esgf-index1.ceda.ac.uk/>) and are freely available. References for the simulations used are in the online supplemental material. The binned North Atlantic subpolar surface salinity data were made freely available by the French Sea Surface Salinity Observation Service (<http://www.legos.obs-mip.fr/observations/sss/>). ERSST was freely available from the National Centers for Environmental Information (<https://www.ncei.noaa.gov/>). The Berkeley Earth Surface Temperature dataset was downloaded from <https://berkeleyearth.org/data/>.

REFERENCES

- Andrews, M. B., and Coauthors, 2020: Historical simulations with HadGEM3-GC3.1 for CMIP6. *J. Adv. Model. Earth Syst.*, **12**, e2019MS001995, <https://doi.org/10.1029/2019MS001995>.
- Andrews, T., R. A. Betts, B. B. Booth, C. D. Jones, and G. S. Jones, 2017: Effective radiative forcing from historical land use change. *Climate Dyn.*, **48**, 3489–3505, <https://doi.org/10.1007/s00382-016-3280-7>.
- Bellomo, K., M. Angeloni, S. Corti, and J. von Hardenberg, 2021: Future climate change shaped by inter-model differences in Atlantic meridional overturning circulation response. *Nat. Commun.*, **12**, 3659, <https://doi.org/10.1038/s41467-021-24015-w>.
- Blaker, A. T., J. J.-M. Hirschi, G. McCarthy, B. Sinha, S. Taws, R. Marsh, A. Coward, and B. de Cuevas, 2015: Historical analogues of the recent extreme minima observed in the Atlantic meridional overturning circulation at 26°N. *Climate Dyn.*, **44**, 457–473, <https://doi.org/10.1007/s00382-014-2274-6>.
- Bonnet, R., and Coauthors, 2021: Increased risk of near term global warming due to a recent AMOC weakening. *Nat. Commun.*, **12**, 6108, <https://doi.org/10.1038/s41467-021-26370-0>.
- Buckley, M. W., and J. Marshall, 2016: Observations, inferences, and mechanisms of the Atlantic meridional overturning circulation: A review. *Rev. Geophys.*, **54**, 5–63, <https://doi.org/10.1002/2015RG000493>.
- Caesar, L., S. Rahmstorf, A. Robinson, G. Feulner, and V. Saba, 2018: Observed fingerprint of a weakening Atlantic Ocean overturning circulation. *Nature*, **556**, 191–196, <https://doi.org/10.1038/s41586-018-0006-5>.
- , G. McCarthy, D. J. R. Thornalley, N. Cahill, and S. Rahmstorf, 2021: Current Atlantic meridional overturning circulation weakest in last millennium. *Nat. Geosci.*, **14**, 118–120, <https://doi.org/10.1038/s41561-021-00699-z>.
- Cai, W., D. Bi, J. Church, T. Cowan, M. Dix, and L. Rotstayn, 2006: Pan-oceanic response to increasing anthropogenic aerosols: Impacts on the Southern Hemisphere oceanic circulation. *Geophys. Res. Lett.*, **33**, L21707, <https://doi.org/10.1029/2006GL027513>.
- Cheng, W., J. C. H. Chiang, and D. Zhang, 2013: Atlantic meridional overturning circulation (AMOC) in CMIP5 models: RCP and historical simulations. *J. Climate*, **26**, 7187–7197, <https://doi.org/10.1175/JCLI-D-12-00496.1>.
- Couldrey, M. P., and Coauthors, 2021: What causes the spread of model projections of ocean dynamic sea-level change in response to greenhouse gas forcing? *Climate Dyn.*, **56**, 155–187, <https://doi.org/10.1007/s00382-020-05471-4>.
- Delworth, T. L., and K. W. Dixon, 2006: Have anthropogenic aerosols delayed a greenhouse gas-induced weakening of the North Atlantic thermohaline circulation? *Geophys. Res. Lett.*, **33**, L02606, <https://doi.org/10.1029/2005GL024980>.
- , and F. Zeng, 2016: The impact of the North Atlantic oscillation on climate through its influence on the Atlantic meridional overturning circulation. *J. Climate*, **29**, 941–962, <https://doi.org/10.1175/JCLI-D-15-0396.1>.
- , S. Manabe, and R. Stouffer, 1993: Interdecadal variations of the thermohaline circulation in a coupled ocean–atmosphere model. *J. Climate*, **6**, 1993–2011, [https://doi.org/10.1175/1520-0442\(1993\)006<1993:IVOTTC>2.0.CO;2](https://doi.org/10.1175/1520-0442(1993)006<1993:IVOTTC>2.0.CO;2).
- Dickson, R. R., J. Meincke, S.-A. Malmberg, and A. J. Lee, 1988: The “great salinity anomaly” in the northern North Atlantic 1968–1982. *Prog. Oceanogr.*, **20**, 103–151, [https://doi.org/10.1016/0079-6611\(88\)90049-3](https://doi.org/10.1016/0079-6611(88)90049-3).
- Dittus, A. J., E. Hawkins, L. J. Wilcox, R. T. Sutton, C. J. Smith, M. B. Andrews, and P. M. Forster, 2020: Sensitivity of historical climate simulations to uncertain aerosol forcing. *Geophys. Res. Lett.*, **47**, e2019GL085806, <https://doi.org/10.1029/2019GL085806>.
- , —, J. I. Robson, D. M. Smith, and L. J. Wilcox, 2021: Drivers of recent North Pacific decadal variability: The role of aerosol forcing. *Earth's Future*, **9**, e2021EF002249, <https://doi.org/10.1029/2021EF002249>.
- Eyring, V., S. Bony, G. A. Meehl, C. A. Senior, B. Stevens, R. J. Stouffer, and K. E. Taylor, 2016: Overview of the Coupled Model Intercomparison Project phase 6 (CMIP6) experimental design and organization. *Geosci. Model Dev.*, **9**, 1937–1958, <https://doi.org/10.5194/gmd-9-1937-2016>.
- Fiedler, S., and D. Putrasahan, 2021: How does the North Atlantic SST pattern respond to anthropogenic aerosols in the 1970s and 2000s? *Geophys. Res. Lett.*, **48**, e2020GL092142, <https://doi.org/10.1029/2020GL092142>.
- Flynn, C. M., and T. Mauritsen, 2020: On the climate sensitivity and historical warming evolution in recent coupled model ensembles. *Atmos. Chem. Phys.*, **20**, 7829–7842, <https://doi.org/10.5194/acp-20-7829-2020>.

- Gillett, N. P., and Coauthors, 2016: The Detection and Attribution Model Intercomparison Project (DAMIP v1.0) contribution to CMIP6. *Geosci. Model Dev.*, **9**, 3685–3697, <https://doi.org/10.5194/gmd-9-3685-2016>.
- Gregory, J. M., and Coauthors, 2016: The Flux-Anomaly-Forced Model Intercomparison Project (FAFMIP) contribution to CMIP6: Investigation of sea-level and ocean climate change in response to CO₂ forcing. *Geosci. Model Dev.*, **9**, 3993–4017, <https://doi.org/10.5194/gmd-9-3993-2016>.
- Grieffes, S. M., and Coauthors, 2014: An assessment of global and regional sea level for years 1993–2007 in a suite of interannual CORE-II simulations. *Ocean Modell.*, **78**, 35–89, <https://doi.org/10.1016/j.ocemod.2014.03.004>.
- Grist, J. P., S. A. Josey, R. Marsh, Y.-O. Kwon, R. J. Bingham, and A. T. Blaker, 2014: The surface-forced overturning of the North Atlantic: Estimates from modern era atmospheric reanalysis datasets. *J. Climate*, **27**, 3596–3618, <https://doi.org/10.1175/JCLI-D-13-00070.1>.
- Hassan, T., R. J. Allen, W. Liu, and C. A. Randles, 2021: Anthropogenic aerosol forcing of the Atlantic meridional overturning circulation and the associated mechanisms in CMIP6 models. *Atmos. Chem. Phys.*, **21**, 5821–5846, <https://doi.org/10.5194/acp-21-5821-2021>.
- Huang, B., and Coauthors, 2017: Extended Reconstructed Sea Surface Temperature, version 5 (ERSSTv5): Upgrades, validations, and intercomparisons. *J. Climate*, **30**, 8179–8205, <https://doi.org/10.1175/JCLI-D-16-0836.1>.
- Jackson, L. C., and Coauthors, 2020: Impact of ocean resolution and mean state on the rate of AMOC weakening. *Climate Dyn.*, **55**, 1711–1732, <https://doi.org/10.1007/s00382-020-05345-9>.
- , A. Biastoch, M. W. Buckley, D. G. Desbruyères, E. Frajka-Williams, B. Moat, and J. Robson, 2022: The evolution of the North Atlantic meridional overturning circulation since 1980. *Nat. Rev. Earth Environ.*, **3**, 241–254, <https://doi.org/10.1038/s43017-022-00263-2>.
- Joshi, M. M., J. M. Gregory, M. J. Webb, D. M. H. Sexton, and T. C. Johns, 2008: Mechanisms for the land/sea warming contrast exhibited by simulations of climate change. *Climate Dyn.*, **30**, 455–465, <https://doi.org/10.1007/s00382-007-0306-1>.
- Kang, S. M., S.-P. Xie, C. Deser, and B. Xiang, 2021: Zonal mean and shift modes of historical climate response to evolving aerosol distribution. *Sci. Bull.*, **66**, 2405–2411, <https://doi.org/10.1016/j.scib.2021.07.013>.
- Kostov, Y., K. C. Armour, and J. Marshall, 2014: Impact of the Atlantic meridional overturning circulation on ocean heat storage and transient climate change. *Geophys. Res. Lett.*, **41**, 2108–2116, <https://doi.org/10.1002/2013GL058998>.
- Large, W. G., and S. G. Yeager, 2009: The global climatology of an interannually varying air–sea flux data set. *Climate Dyn.*, **33**, 341–364, <https://doi.org/10.1007/s00382-008-0441-3>.
- Lawrence, D. M., and Coauthors, 2016: The Land Use Model Intercomparison Project (LUMIP) contribution to CMIP6: Rationale and experimental design. *Geosci. Model Dev.*, **9**, 2973–2998, <https://doi.org/10.5194/gmd-9-2973-2016>.
- Lund, M. T., G. Myhre, and B. H. Samset, 2019: Anthropogenic aerosol forcing under the shared socioeconomic pathways. *Atmos. Chem. Phys.*, **19**, 13 827–13 839, <https://doi.org/10.5194/acp-19-13827-2019>.
- Ma, L., T. Woollings, R. G. Williams, D. Smith, and N. Dunstone, 2020: How does the winter jet stream affect surface temperature, heat flux, and sea ice in the North Atlantic? *J. Climate*, **33**, 3711–3730, <https://doi.org/10.1175/JCLI-D-19-0247.1>.
- Marshall, J., A. Donohoe, D. Ferreira, and D. McGee, 2014: The ocean's role in setting the mean position of the Inter-Tropical Convergence Zone. *Climate Dyn.*, **42**, 1967–1979, <https://doi.org/10.1007/s00382-013-1767-z>.
- Megann, A., A. Blaker, S. Josey, A. New, and B. Sinha, 2021: Mechanisms for late 20th and early 21st century decadal AMOC variability. *J. Geophys. Res. Oceans*, **126**, e2021JC017865, <https://doi.org/10.1029/2021JC017865>.
- Menary, M. B., and A. A. Scaife, 2014: Naturally forced multidecadal variability of the Atlantic meridional overturning circulation. *Climate Dyn.*, **42**, 1347–1362, <https://doi.org/10.1007/s00382-013-2028-x>.
- , and Coauthors, 2013: Mechanisms of aerosol-forced AMOC variability in a state of the art climate model. *J. Geophys. Res. Oceans*, **118**, 2087–2096, <https://doi.org/10.1002/jgrc.20178>.
- , D. L. R. Hodson, J. I. Robson, R. T. Sutton, R. A. Wood, and J. A. Hunt, 2015: Exploring the impact of CMIP5 model biases on the simulation of North Atlantic decadal variability. *Geophys. Res. Lett.*, **42**, 5926–5934, <https://doi.org/10.1002/2015GL064360>.
- , and Coauthors, 2020: Aerosol-forced AMOC changes in CMIP6 historical simulations. *Geophys. Res. Lett.*, **47**, e2020GL088166, <https://doi.org/10.1029/2020GL088166>.
- Moat, B. I., and Coauthors, 2019: Insights into decadal North Atlantic sea surface temperature and ocean heat content variability from an eddy-permitting coupled climate model. *J. Climate*, **32**, 6137–6161, <https://doi.org/10.1175/JCLI-D-18-0709.1>.
- Otterå, O. H., M. Bentsen, H. Drange, and L. Suo, 2010: External forcing as a metronome for Atlantic multidecadal variability. *Nat. Geosci.*, **3**, 688–694, <https://doi.org/10.1038/ngeo955>.
- Petit, T., M. S. Lozier, S. A. Josey, and S. A. Cunningham, 2021: Role of air–sea fluxes and ocean surface density in the production of deep waters in the eastern subpolar gyre of the North Atlantic. *Ocean Sci.*, **17**, 1353–1365, <https://doi.org/10.5194/os-17-1353-2021>.
- Polo, I., J. Robson, R. Sutton, and M. A. Balmaseda, 2014: The importance of wind and buoyancy forcing for the boundary density variations and the geostrophic component of the AMOC at 26°N. *J. Phys. Oceanogr.*, **44**, 2387–2408, <https://doi.org/10.1175/JPO-D-13-0264.1>.
- Reverdin, G., A. R. Friedman, L. Chafik, N. P. Holliday, T. Szekely, H. Valdimarsson, and I. Yashayaev, 2019: North Atlantic extratropical and subpolar gyre variability during the last 120 years: A gridded dataset of surface temperature, salinity, and density. Part 1: Dataset validation and RMS variability. *Ocean Dyn.*, **69**, 385–403, <https://doi.org/10.1007/s10236-018-1240-y>.
- Robson, J., R. Sutton, K. Lohmann, D. Smith, and M. D. Palmer, 2012: Causes of the rapid warming of the North Atlantic Ocean in the mid-1990s. *J. Climate*, **25**, 4116–4134, <https://doi.org/10.1175/JCLI-D-11-00443.1>.
- , and Coauthors, 2020: The evaluation of the North Atlantic climate system in UKESM1 historical simulations for CMIP6. *J. Adv. Model. Earth Syst.*, **12**, e2020MS002126, <https://doi.org/10.1029/2020MS002126>.
- Rohde, R. A., and Z. Hausfather, 2020: The Berkeley Earth land/ocean temperature record. *Earth Syst. Sci. Data*, **12**, 3469–3479, <https://doi.org/10.5194/essd-12-3469-2020>.
- Sarmiento, J. L., and C. Le Quéré, 1996: Oceanic carbon dioxide uptake in a model of century-scale global warming. *Science*, **274**, 1346–1350, <https://doi.org/10.1126/science.274.5291.1346>.

- Scaife, A. A., and D. Smith, 2018: A signal-to-noise paradox in climate science *npj Climate Atmos. Sci.*, **1**, 28, <https://doi.org/10.1038/s41612-018-0038-4>.
- Schulzweida, U., 2021: CDO user guide. Version 1.9.5, Zenodo, accessed 9 August 2008, <https://doi.org/10.5281/zenodo.5614769>
- Sévellec, F., A. V. Fedorov, and W. Liu, 2017: Arctic sea-ice decline weakens the Atlantic meridional overturning circulation. *Nat. Climate Change*, **7**, 604–610, <https://doi.org/10.1038/nclimate3353>.
- Smith, C. J., and Coauthors, 2021: Energy budget constraints on the time history of aerosol forcing and climate sensitivity. *J. Geophys. Res. Atmos.*, **126**, e2020JD033622, <https://doi.org/10.1029/2020JD033622>.
- Speer, K., and E. Tziperman, 1992: Rates of water mass formation in the North Atlantic Ocean. *J. Phys. Oceanogr.*, **22**, 93–104, [https://doi.org/10.1175/1520-0485\(1992\)022<0093:ROWMFI>2.0.CO;2](https://doi.org/10.1175/1520-0485(1992)022<0093:ROWMFI>2.0.CO;2).
- Sutton, R. T., B. Dong, and J. M. Gregory, 2007: Land/sea warming ratio in response to climate change: IPCC AR4 model results and comparison with observations. *Geophys. Res. Lett.*, **34**, L02701, <https://doi.org/10.1029/2006GL028164>.
- , G. D. McCarthy, J. Robson, B. Sinha, A. T. Archibald, and L. J. Gray, 2018: Atlantic multidecadal variability and the U.K. ACSIS program. *Bull. Amer. Meteor. Soc.*, **99**, 415–425, <https://doi.org/10.1175/BAMS-D-16-0266.1>.
- Swart, N. C., and Coauthors, 2019: The Canadian Earth System Model version 5 (CANESM5.0.3). *Geosci. Model Dev.*, **12**, 4823–4873, <https://doi.org/10.5194/gmd-12-4823-2019>.
- Swingedouw, D., P. Ortega, J. Mignot, E. Guilyardi, V. Masson-Delmotte, P. G. Butler, M. Khodri, and R. Séférian, 2015: Bidecadal North Atlantic Ocean circulation variability controlled by timing of volcanic eruptions. *Nat. Commun.*, **6**, 6545, <https://doi.org/10.1038/ncomms7545>.
- Tandon, N. F., and P. J. Kushner, 2015: Does external forcing interfere with the AMOC's influence on North Atlantic sea surface temperature? *J. Climate*, **28**, 6309–6323, <https://doi.org/10.1175/JCLI-D-14-00664.1>.
- Thornalley, D. J. R., and Coauthors, 2018: Anomalously weak Labrador Sea convection and Atlantic overturning during the past 150 years. *Nature*, **556**, 227–230, <https://doi.org/10.1038/s41586-018-0007-4>.
- Trenberth, K. E., Y. Zhang, J. T. Fasullo, and L. Cheng, 2019: Observation-based estimates of global and basin ocean meridional heat transport time series. *J. Climate*, **32**, 4567–4583, <https://doi.org/10.1175/JCLI-D-18-0872.1>.
- Undorf, S., M. A. Bollasina, B. B. Booth, and G. C. Hegerl, 2018: Contrasting the effects of the 1850–1975 increase in sulphate aerosols from North America and Europe on the Atlantic in the CESM. *Geophys. Res. Lett.*, **45**, 11930–11940, <https://doi.org/10.1029/2018GL079970>.
- Walín, G., 1982: On the relation between sea-surface heat flow and thermal circulation in the ocean. *Tellus*, **34**, 187–195, <https://doi.org/10.3402/tellusa.v34i2.10801>.
- Wang, C., L. Zhang, S.-K. Lee, L. Wu, and C. R. Mechoso, 2014: A global perspective on CMIP5 climate model biases. *Nat. Climate Change*, **4**, 201–205, <https://doi.org/10.1038/nclimate2118>.
- , B. J. Soden, W. Yang, and G. A. Vecchi, 2021: Compensation between cloud feedback and aerosol–cloud interaction in CMIP6 models. *Geophys. Res. Lett.*, **48**, e2020GL091024, <https://doi.org/10.1029/2020GL091024>.
- Wang, Y., J. H. Jiang, and H. Su, 2015: Atmospheric responses to the redistribution of anthropogenic aerosols. *J. Geophys. Res. Atmos.*, **120**, 9625–9641, <https://doi.org/10.1002/2015JD023665>.
- Weijer, W., W. Cheng, O. A. Garuba, A. Hu, and B. T. Nadiga, 2020: CMIP6 models predict significant 21st century decline of the Atlantic meridional overturning circulation. *Geophys. Res. Lett.*, **47**, e2019GL086075, <https://doi.org/10.1029/2019GL086075>.
- Wilcox, L. J., E. J. Highwood, and N. J. Dunstone, 2013: The influence of anthropogenic aerosol on multi-decadal variations of historical global climate. *Environ. Res. Lett.*, **8**, 024033, <https://doi.org/10.1088/1748-9326/8/2/024033>.
- Xu, X., E. P. Chassignet, and F. Wang, 2019: On the variability of the Atlantic meridional overturning circulation transports in coupled CMIP5 simulations. *Climate Dyn.*, **52**, 6511–6531, <https://doi.org/10.1007/s00382-018-4529-0>.
- Yan, X., R. Zhang, and T. R. Knutson, 2018: Underestimated AMOC variability and implications for AMV and predictability in CMIP models. *Geophys. Res. Lett.*, **45**, 4319–4328, <https://doi.org/10.1029/2018GL077378>.
- Yeager, S., and Coauthors, 2021: An oversized role for the Labrador Sea in the multidecadal variability of the Atlantic overturning circulation. *Sci. Adv.*, **7**, eabh3592, <https://doi.org/10.1126/sciadv.abh3592>.
- Yin, J., M. E. Schlesinger, and R. J. Stouffer, 2009: Model projections of rapid sea-level rise on the northeast coast of the United States. *Nat. Geosci.*, **2**, 262–266, <https://doi.org/10.1038/ngeo462>.
- Zelinka, M. D., T. Andrews, P. M. Forster, and K. E. Taylor, 2014: Quantifying components of aerosol–cloud–radiation interactions in climate models. *J. Geophys. Res. Atmos.*, **119**, 7599–7615, <https://doi.org/10.1002/2014JD021710>.
- Zhang, J., and Coauthors, 2021: The role of anthropogenic aerosols in the anomalous cooling from 1960 to 1990 in the CMIP6 Earth system models. *Atmos. Chem. Phys.*, **21**, 18609–18627, <https://doi.org/10.5194/acp-21-18609-2021>.
- Zhang, R., and M. Thomas, 2021: Horizontal circulation across density surfaces contributes substantially to the long-term mean northern Atlantic meridional overturning circulation. *Commun. Earth Environ.*, **2**, 112, <https://doi.org/10.1038/s43247-021-00182-y>.
- , R. Sutton, G. Danabasoglu, Y.-O. Kwon, R. Marsh, S. G. Yeager, D. E. Amrhein, and C. M. Little, 2019: A review of the role of the Atlantic meridional overturning circulation in Atlantic multidecadal variability and associated climate impacts. *Rev. Geophys.*, **57**, 316–375, <https://doi.org/10.1029/2019RG000644>.
- Zhu, C., and Z. Liu, 2020: Weakening Atlantic overturning circulation causes South Atlantic salinity pile-up. *Nat. Climate Change*, **10**, 998–1003, <https://doi.org/10.1038/s41558-020-0897-7>.